The Influence of Reconstruction and Attenuation Correction Techniques on the detection of hypo-perfused lesions in Brain SPECT Images

Shivani Ghoorun

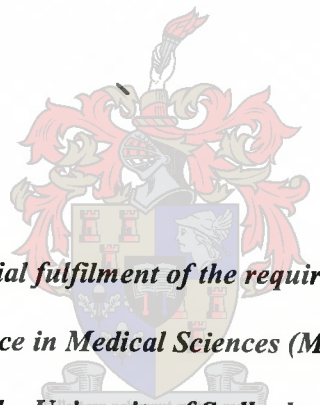

Thesis presented in partial fulfilment of the requirements for the degree of

Master of Science in Medical Sciences (Medical Physics)

at the University of Stellenbosch

Supervisors: Dr WA Groenewald
Prof J Nuyts

April 2004

"***Declaration***

I, the undersigned, hereby declare that the work contained in this thesis is my own original work and that I have not previously in its entirety or in part submitted it at any university for a degree.

Signature:_____ Date:_____"

Summary

Functional brain imaging using single photon emission computed tomography (SPECT) has widespread applications in the case of Alzheimers disease, acute stroke, transient ischaemic attacks, epilepsy, recurrent primary tumours and head trauma. Routine clinical SPECT imaging utilises uniform attenuation correction, assuming that the head has homogeneous attenuation properties and elliptical cross-sections. This method may be improved upon by using an attenuation map which more accurately represents the spatial distribution of linear attenuation coefficients in the brain.

Reconstruction of the acquired projection data is generally performed using filtered backprojection (FBP). This is known to produce unwanted streak artifacts. Iterative techniques such as maximum likelihood (ML) methods have also been proposed to improve the reconstruction of tomographic data. However, long computation times have limited its use.

In this investigation, the objective was to determine the influence of different attenuation correction and reconstruction techniques on the detection of hypo-perfused lesions in brain SPECT images.

The study was performed as two simulation experiments, formulated to decouple the effects of attenuation and reconstruction. In the first experiment, a high resolution SPECT phantom was constructed from four high resolution MRI scans by segmenting the MRI data into white matter, grey matter and cerebrospinal fluid (CSF). Appropriate intensity values were then assigned to each tissue type. A true

attenuation map was generated by transposing the 511 keV photons of a PET transmission scan to 140 keV photons of SPECT. This method was selected because transmission scanning represents the gold standard for determining attenuation coefficients.

The second experiment utilised an available digital phantom with the tissue classes already segmented. The primary difference between the two experiments was that in Experiment II, the attenuation map used for the creation of the phantom was clinically more realistic by using MRI data that were segmented into nine tissue classes. In this case, attenuation coefficients were assigned to each tissue class to create a non-uniform attenuation map. A uniform attenuation map was generated on the basis of emission projections for both experiments.

Hypo-perfused lesions of varying intensities and sizes were added to the phantom. The phantom was then projected as typical SPECT projection data, taking into account attenuation and collimator blurring with the addition of Poisson noise.

Each experiment employed four methods of reconstruction: (1) FBP with the uniform attenuation map; (2) FBP using the true attenuation map; (3) ML method with a uniform attenuation map; and (4) ML method with a true attenuation map. In the case of FBP methods, Chang's first order attenuation correction was used.

The analysis of the reconstructed data was performed using figures of merit such as signal to noise ratio (SNR), bias and variance. The results illustrated that uniform attenuation correction offered slight deterioration (less than 2 %) with regard to

detection of lesions when compared to the ideal attenuation map, which in reality is not known.

The reconstructions demonstrated that FBP methods underestimated the activity by more than 30% when compared to the true image. The iterative techniques produced superior signal to noise ratios in comparison to the FBP methods, provided that postsmoothing was applied to the data. The results also showed that the iterative methods produced lower bias at the same variance.

This leads to the conclusion, that in the case of brain SPECT imaging, uniform attenuation correction is adequate for lesion detection. In addition, iterative reconstruction techniques provide enhanced lesion detection when compared to filtered backprojection methods.

Opsomming

Funksionele breinbeelding deur middel van Enkel Foton Emissie Rekenaartomografie (SPECT – Single Photon Emission Computed Tomography) het veelvuldige toepassings in die geval van Alzheimer se siekte, akute beroerte, kortstondige isgemiese aanvalle, epilepsie, hervatting van primêre tumore en hoofbeserings. Roetine kliniese SPECT-beelding gebruik uniforme attenuasie korreksies met die aanname dat die kop homogene attenuasie eienskappe en elliptiese dwarssnitte het. Hierdie metode kan verbeter word deur die gebruik van 'n attenuasiekaart wat 'n akkurater weergawe van die ruimtelike verspreiding van lineêre attenuasie koëffisiënte in die brein verteenwoordig.

Rekonstruksie van die ingesamelde projeksiedata word gewoonlik uitgevoer deur gebruik te maak van Gefiltreerde Terugprojeksie (FBP – Filtered Backprojection). Dit is bekend dat hierdie tegniek ongewenste streep artefakte veroorsaak. Iteratiewe tegnieke soos maksimum waarskynlikheid (ML – Maximum Likelihood) metodes is ook voorgestel om die rekonstruksie van tomografiese data te verbeter. Lang berekeningstye het tot dusver die gebruik van hierdie tegnieke beperk.

Die doelstelling van hierdie ondersoek was om die invloed van verskillende attenuasie korreksie en rekonstruksie tegnieke op letsels met hipo-perfusie in brein SPECT beelde te bepaal.

Die ondersoek is uitgevoer in die vorm van twee simulasie eksperimente, en is geformuleer om die effekte van attenuasie en rekonstruksie te ontkoppel. In die eerste eksperiment is 'n hoë resolusie SPECT fantoom uit vier hoë resolusie MRI (Magnetic

Resonance Imaging) beelde gekonstrueer deur die MRI data in wit stof, grys stof en CSF (Cerebrospinal Fluid) te segmenteer. Geskikte intensiteitswaardes is aan elke weefseltipe toegeken. 'n Ware attenuasiekaart is geskep deur die 511 keV fotone van 'n PET (Positron Emission Tomography) transmissie opname na 140 keV fotone van SPECT te transponeer. Hierdie metode is gekies aangesien transmissie skandering die goue standaard vir die bepaling van attenuasie koëffisiënte verteenwoordig.

Die tweede eksperiment het 'n beskikbare digitale fantoom gebruik met die weefsel soorte reeds gesegmenteer. Die primêre verskil tussen die twee eksperimente was dat die attenuasiekaart gebruik in eksperiment II klinies meer realisties was, aangesien MRI data gebruik is wat reeds in nege weefselsoorte gesegmenteer is. Attenuasie koëffisiënte is aan elke weefselsoort toegeken om 'n nie-uniforme attenuasiekaart saam te stel. 'n Uniforme attenuasiekaart gebaseer op die emissie projeksies vir beide eksperimente is saamgestel.

Hipo-perfusie letsels met verskillende intensiteite en groottes is by die fantoom gevoeg. Die fantoom is daarna geprojekteer as tipiese SPECT projeksiedata met inagneming van attenuasie en kollimator versluiering met die toevoeging van Poisson geraas.

Elke eksperiment het vier metodes van rekonstruksie gebruik: (1) FBP met die uniforme attenuasiekaart; (2) FBP met gebruik van die ware attenuasiekaart; (3) die ML-metode met 'n uniforme attenuasiekaart; en (4) die ML-metode met 'n ware attenuasiekaart. Chang se eerste orde attenuasie korreksie is in die geval van die FBP-metodes gebruik.

Die ontleding van die gerekonstrueerde data is gedoen deur verdienstesyfers soos sein-tot-geraas verhouding (SNR), sydigheid en variansie te gebruik. Die resultate toon dat die uniforme attenuasiekorreksie 'n geringe verswakking (minder as 2 %) gee met betrekking tot die opsporing van letsels wanneer 'n vergelyking met die ideale attenuasiekaart, wat nie bekend is nie, getref word. Die rekonstruksies demonstreer dat die FBP metodes die aktiwiteit met meer as 30% onderskat in vergelyking met die ware beeld. Die iteratiewe tegnieke het uitstekende sein-tot-geraas verhoudings gelewer in vergelyking met die FBP-metodes op voorwaarde dat na-vergladding op die data toegepas is. Die resultate het ook getoon dat die iteratiewe metodes laer sydigheid by dieselfde variansie lewer.

Die slotsom is dat, in die geval van brein SPECT beelding, uniforme attenuasiekorreksie voldoende is vir letselopsporing. Die iteratiewe rekonstruksie tegnieke bied verder verbeterde letselopsporing in vergelyking met gefiltreerde terugprojeksie metodes.

Acknowledgements

Two weeks before submission, the point of convergence was still not in sight. Many people kept me inspired and motivated and for this I will be forever grateful.

One of my great personal joys was the opportunity to work with my supervisor, *Professor Johan Nuyts* from KU Leuven, Belgium, the world guru on image reconstruction. Johan introduced me to the wonders of IDL programming, he made available his extensive range of IDL sources, he shared his knowledge and ideas, he entertained me with his lecture notes on image reconstruction, and the list continues... Johan, none of this would have been possible without your perceptive guidance.

Dr Wilhelm Groenewald, my boss and supervisor at Tygerberg Hospital, stands as a rock of integrity. He followed my progress closely from the beginning, painstakingly read through each chapter, provided helpful recommendations and ensured that I met the deadline. Dr Groenewald, you've assisted me in more ways than you realise.

Thanks to the staff at Nucleaire Geneeskunde, KU Leuven, for warmly welcoming me into their family. I am grateful to *Francine Reniers*, for so efficiently handling the administration of my several trips to Belgium; to *Ina Van t'Velt* and *Ann Casimmons*, my friends, for helping me balance work and play. Special thanks to *Kristof Baete*, my office mate, for helping me login and logout, for sharing his brainweb data and IDL knowledge and for encouraging me when my code would not compile. This list will be incomplete if I do not mention *Erik Nolf*, the xmedcon man, from University of Ghent. He taught me more than the finer points of Linux and cshell scripting; he taught me that the only approach to life is with a vibrant spirit.

I owe many thanks to every one of my friends and colleagues at Tygerberg Hospital and the Cape. A personal acknowledgement to each of you would be ideal, but I fear the consequence of any omissions. Your support and understanding, especially in the last days, were greatly appreciated.

I am grateful to my old school pal *Dr Lester John* from Medical Imaging, UCT who, despite his demanding schedule, meticulously proofread the thesis and provided helpful suggestions before the final compilation.

To my parents, for pointing my compass in the moral direction, regardless of trends. To the rest of my family, for enriching me with love and wisdom.

When special people touch our lives, we see how beautiful and wonderful the world can really be. *Professor Patrick Dupont*, from KU Leuven, Belgium invited me to participate in his research activities on brain imaging in the year 2000, which sparked an alliance that will surely last a lifetime. Patrick was the initiator of this project; many of the ideas evolved from the marvels of his brain. He spent several hours coaching and inspiring me. He enthusiastically followed my work and miraculously found the time to scrutinise every word in this thesis. Patrick, thank you for believing in me...

Shivani

Acronyms

1-D	one-dimensional
2-D	two-dimensional
3-D	three-dimensional
CT	computed tomography
EM	expectation maximisation
FBP	filtered backprojection
FBP-true	FBP using the true attenuation map
FBP-unif	FBP using the uniform attenuation map
FWHM	full width at half maximum
HMPAO	Hexa-methylpropylene amine oxime
IDL	interactive data language
ML	maximum likelihood
ML-true	ML using the true attenuation map
ML-unif	ML using a uniform attenuation map
MRI	magnetic resonance imaging
NaI(Tl)	thallium-activated sodium iodide
OSEM	ordered subset expectation maximisation
PET	positron emission tomography
PHA	pulse height analyser
rCBF	regional cerebral blow flow
rms	root mean squared
ROI	region of interest
SNR	signal to noise ratio
SPECT	single photon emission computed tomography

Table of Contents

Chapter 1

Introduction

Functional brain imaging is a technique used to derive images reflecting biochemical or physiologic properties of the Central Nervous System. The developed techniques in this field are single photon emission computed tomography (SPECT), positron emission tomography (PET) and functional magnetic resonance imaging (MRI). Tomography permits visualisation of the three dimensional tracer distribution of an object as a series of thin section images and this can provide several clinical advantages in the case of functional imaging.

1.1 Functional Brain Imaging

The applications of functional imaging of the brain were clearly outlined by Holman *et al* [1] in his paper entitled "Functional Brain SPECT: The Emergence of a Powerful Clinical Method". The relevance of regional cerebral blood flow (rCBF) SPECT imaging in stroke, transient ischaemic attacks and other problems with cerebral haemodynamics were described. In addition, the role of SPECT in localising epileptic focus is a well established technique. The paper by Holman [1] lists the widely accepted uses of Brain SPECT. These include Alzheimers disease, acute stroke, transient ischaemic attacks, epilepsy, recurrent primary tumours and head trauma.

The clinical value of brain perfusion SPECT is discussed by Catafu *et al* [2]. SPECT is described as being "sensitive in detecting impairment of regional cerebral function when CT or MRI shows only non-specific findings such as cerebral atrophy".

While functional brain imaging has significant clinical applications, quantification poses certain difficulties due to reconstruction and attenuation correction issues. The method of filtered backprojection (FBP) has been widely used in SPECT reconstruction, often in combination with attenuation correction techniques. The primary reason for this is the short computation times and ease of implementation. However, this method produces unwanted streak artifacts and the final image is an approximation and therefore not very accurate.

Different reconstruction algorithms need to be explored, especially in the case of brain imaging where quantification is necessary. It has been suggested that reconstruction can be improved using iterative techniques since noise, attenuation and scatter effects can be included in such reconstruction algorithms.

Attenuation correction routinely used for brain SPECT imaging assumes that the brain is homogeneous, therefore a uniform value for the attenuation coefficient is used. Uniform attenuation coefficients make no compensation for attenuation due to the surrounding skull.

1.2 Literature Review

Attenuation Correction

Reconstruction of tomographic images without attenuation correction or with incorrect attenuation correction can cause artificially high or low count densities and inaccurate contrast. In the uncorrected image, the reconstructed activity at the centre of the brain tends to be decreased. These artifacts can complicate visual interpretation

and cause profound accuracy errors which can become especially detrimental when radionuclide images are evaluated quantitatively.

Reliable attenuation correction methods for emission tomography require accurate determination of an attenuation map. This map represents the spatial distribution of linear attenuation coefficients for different regions of the patient's anatomy. Broadly, there are two classes of methods for generating the attenuation map. The first class is based on calculated methods, where the boundaries and distributions are estimated from the emission data. The second class is based on an additional measurement. These include transmission scanning using an external radionuclide source, Computed Tomography (CT) or segmented MRI images.

The calculated methods assume a known body contour with a uniform distribution of attenuation coefficients. Licho *et al* [3] investigated the use of different attenuation maps for ^{99m}Tc brain SPECT imaging. In this study, four methods were compared, namely: (a) attenuation map obtained from transmission scanning; (b) attenuation map derived from a lower energy Compton scatter window; (c) slice independent, uniform elliptical attenuation map; and (d) no attenuation correction. Count profiles showed significant differences in regional count estimates amongst the different methods. This study suggested that clinical ^{99m}Tc brain perfusion SPECT benefits from transmission-based attenuation correction. This study also reported that uniform attenuation corrected studies provided unreliable regional estimates of tracer activity.

Larsson *et al* [4] presented a method for the conversion of Hounsfield numbers to attenuation coefficients for 140 keV photons from ^{99m}Tc. The accuracy of the

quantitative results was highly dependent on how closely the CT image volume could be fitted to the SPECT image volume. However, comparing this to a method where an image volume was corrected with a homogeneous attenuation map showed small differences for rCBF measurements. The non-uniform attenuation map was obtained by matching CT images to SPECT or through a transmission scan performed with a gamma camera. This study demonstrated that the use of a homogeneous attenuation map only caused little loss in accuracy.

The paper by Bailey [5] stated that the most accurate attenuation correction methods are based on measured transmission scans acquired before, during, or after the emission scan. He observed that transmission scanning often lead to high noise in the attenuation correction data which was transferred to the final reconstructed emission images. It is recommended that the transmission data require some processing to suppress the noise.

A comparison of non-uniform versus uniform attenuation correction in brain perfusion SPECT was performed by Van Laere *et al* [6]. This study compared the use of transmission based methods to Sorenson's method [7] and non-uniform Chang attenuation correction algorithm [8]. This study demonstrated that differences between non-uniform and uniform attenuation are small. In the infra-tentorial region, where marked inhomogeneous attenuation is present, small but significant changes were found.

Another approach to constructing a reliable attenuation map is to use MRI data. This method is described by Rowell *et al* [9] where attenuation corrections were obtained

by considering paths representing photon emissions from a central position in the region of interest. By measuring the distance travelled through each type of attenuating medium, an effective attenuation coefficient was calculated for each photon path. This study established that the attenuation coefficients obtained from CT and MRI images were not significantly different from that obtained using a ^{57}Co flood source. The study concluded that information derived from CT or MRI provided a suitable alternative to transmission scanning for determining the attenuation map.

Zaidi *et al* [10] aligned the MR images to PET reconstructed data and segmented the MR image to identify tissues of significantly different density and composition. The voxels belonging to different regions were classified into air, skull, brain tissue and nasal sinuses. These voxels were assigned theoretical tissue dependent attenuation coefficients. The results were validated on 10 patients with transmission and MRI images. The use of the segmented MRI image demonstrated a clear improvement in image quality due to the reduction of the noise propagation from the transmission into the emission data.

From the preceding overview, some findings demonstrate that only small improvements can be achieved with the use of a non-uniform attenuation map, while others strongly advocate its use to avoid unreliable regional estimates of tracer activity.

Image Reconstruction

Since the late 1970's, the advantages of iterative reconstruction methods have been discussed in the literature. The application of maximum likelihood (ML) reconstruction in the medical field was developed by Shepp and Vardi [11] and by Lange and Carson [12] independently. Both papers utilised the expectation maximization (EM) approach described by Dempster [13].

ML and FBP methods were compared in a study by Chornoboy *et al* [14]. The experiment was performed as three simulation studies. In addition, experimental images of acrylic phantoms were acquired to compare the simulation results to the images obtained from a commercially available system. The first experiment involved reconstruction of a bar phantom consisting of four groups of bars of widths 2, 4, 6 and 8 pixels (one pixel = 2.67 mm). Qualitatively, both reconstructions appeared to resolve the three largest sets of bars.

Signal to noise ratios were 3.178 and 3.416 for the FBP and ML methods respectively. The full width at half maximum (FWHM) was 6.26 for the FBP method and 3.12 for the ML method. The large discrepancy in the resolution could be partially attributed to the fact that the ML method deconvolved the point spread response function in the reconstruction, whereas there was no compensation for this in the FBP method.

The second experiment used a solid acrylic rod as well as an air-filled rod. FBP images demonstrated higher noise content than the corresponding ML images. Signal to noise ratios were found to be far superior with the ML methods. In the third

experiment a chest phantom used acrylic, barium and air to simulate soft tissue, bone and lungs respectively. In this experiment, the signal to noise ratios using the ML methods were superior to the FBP methods by a factor of three. The results of these three experiments supported the conclusion that ML methods proved beneficial for SPECT reconstruction in terms of lesion detection, image resolution and quantification.

Kauppinen *et al* [15] evaluated the quantitative accuracy of iterative reconstruction in SPECT brain perfusion imaging. Comparison between organ-like phantom measurements with actual activity values was performed. The results were further validated by analysing patient perfusion studies. This study demonstrated that iterative reconstruction increased the contrast of the image and improved separation between the different regions. The differences from the true image (in the case of the phantom study) were largest with the FBP method. However, this difference was probably exaggerated because the iterative technique used non-uniform attenuation correction derived from a transmission scan, whereas the FBP method used Chang's first order approximation [8] to calculate the attenuation.

Gutman *et al* [16] compared ordered subset expectation maximisation (OSEM) and FBP for image reconstruction on a fluorine-18 fluorodeoxyglucose (^{18}F-FDG) dual head camera. This was performed on phantom as well as patient acquisitions. Contrast recovery coefficients and noise characteristics were assessed. The clinical study showed that OSEM yielded images of better visual quality but no improvement in terms of detection of lung cancer was observed.

FBP and OSEM reconstruction techniques were compared in bone SPECT by Blocklet *et al* [17.]. The quality of the pictures proved to be superior with OSEM in 98 % of the cases and it was recommended that OSEM should replace FBP in clinical practice.

1.3 Objective of the Study

At Tygerberg Hospital, the method of filtered backprojection is the most extensively used reconstruction technique for Brain SPECT studies. In addition, attenuation correction is performed using conventional SPECT processing software where manually drawn contours, or ellipses generated from edge-detection methods, determine the attenuation map. The method assumes that the brain is homogeneous and a fixed attenuation coefficient of 0.11 cm^{-1} is used. This factor compensates for scatter included in the projections, but does not consider the inhomogeneities in the brain structure.

In view of the improvements advocated with iterative techniques and the discrepancies in the literature relating to attenuation correction, further evaluation of the clinical impact of attenuation correction and reconstruction methods is warranted. The aim of this study was to investigate the influence of reconstruction and attenuation correction on the detection of regions of hypo-perfusion in Brain SPECT studies.

Primarily, the focus of this study involved the detection of hypo-perfused lesions in the brain. The study was formulated such that reconstruction and attenuation effects could be evaluated independently to explore two research questions: (1) does iterative

reconstruction improve lesion detection; and (2) does the use of uniform attenuation correction influence the detection of hypo-perfused lesions in brain SPECT studies.

It was hypothesised that the maximum likelihood method of reconstruction would produce superior images. Moreover, uniform attenuation correction would produce decreased lesion detection. The decrease may be more observable in anterior temporal regions and in the cerebellum since the non-uniformity of the attenuation is largest around these regions.

The investigation was performed as two simulation experiments. The basic steps are outlined below:

1. Development of a 3-D software phantom containing hypo-perfused lesions. The software phantom represented a realistic human brain.
2. The phantom was manipulated such that reasonable activity values were assigned to represent lesions of different sizes and signal contrasts.
3. The phantom was projected as SPECT data taking into account attenuation and collimator blurring, with the addition of Poisson noise.
4. The set of projections were reconstructed using different reconstruction and attenuation correction techniques.
5. The generated reconstructed images were compared to the reference image and to each other by computing signal to noise ratios, bias and variance values.

1.4 Chapter Outline

The principles of operation of a SPECT gamma camera are described in **Chapter Two**. The basic electronics of the detector and the factors that degrade the image are explained. **Chapter Three** provides an intuitive as well as rigorous explanation of image reconstruction. Continuous and discrete cases are described.

The materials and methods employed in this investigation are detailed in **Chapter Four**. The construction of the software phantom and the attenuation maps, together with the generation of the projection data and the reconstruction using the different methods are outlined.

Chapter Five presents the results of the two simulation experiments. The phantoms, attenuation maps and reconstructed images are displayed. Curves showing comparative signal to noise ratios and bias and variance relationships are presented.

An in-depth discussion of the results is presented in **Chapter Six**. This is followed by **Chapter Seven** where conclusions are drawn and suggestions for future related research are proposed.

Chapter 2

Single Photon Emission Computed Tomography

2.1 Introduction

Conceptually similar to CT, SPECT is a scanning technique whereby gamma camera images or projections are acquired over a range of angles around a patient. These projections allow the reconstruction of cross sectional (tomographic) images of the organ of interest. Briefly, the procedure of SPECT involves the injection of a gamma-emitting radiopharmaceutical into the patient. The radiopharmaceutical is specific for some physiological function and it accumulates within the organ of interest. The gamma ray photons emitted by the radiopharmaceutical are detected by the scintillation camera, which rotates around the patient. The acquisitions are performed over a number of angles varying from 60 to 120 views, depending on the application. Using the information of the projections, the aim is to compute the three dimensional (3-D) distribution of the radiopharmaceutical.

2.2 The Gamma Camera

2.2.1 Principles of Operation

The fundamental principles of operation of the gamma camera are summarised below [18]:

- The radionuclide distribution, represented by gamma ray photons, is projected onto the thallium-activated sodium iodide (NaI(Tl)) crystal by the collimator.
- The photons interact with the crystal to produce flashes of light or a pattern of scintillations.

- These scintillations are individually converted to current pulses by the array of photomultiplier tubes.
- The electric signals from each photomultiplier tube are processed by the position and energy circuitry to generate the X and Y position signals and the Z-energy signal.
- This energy signal is analysed by the pulse height analyser (PHA). An output signal is only produced if the gamma ray energy falls within a specific range.
- The X and Y position signal increments the digital pixel value in the image corresponding to the location of the scintillation event on the crystal.

2.2.2 The Components

The detector and the processing electronics comprise the main functional unit of the gamma camera. The basic detector consists of a collimator, a thin, large NaI(Tl) crystal, a transparent optical light pipe, an array of photomultiplier tubes, associated preamplifiers and positioning circuitry [19]. The basic components of a gamma camera are displayed in Figure 2.1.

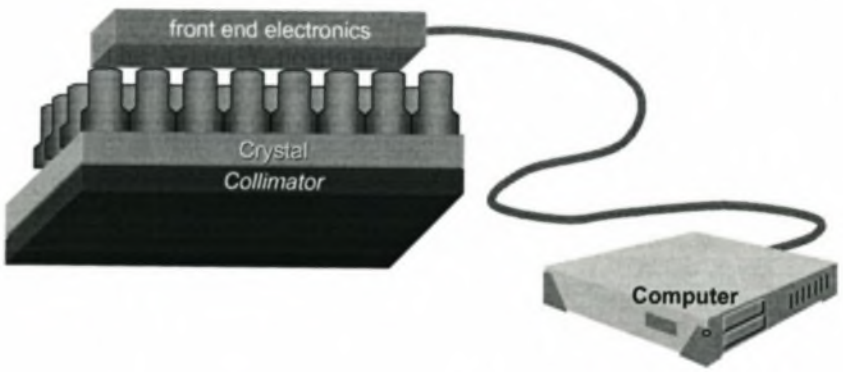

Figure 2.1 Basic components of the gamma camera (Picture courtesy of Professor Johan Nuyts)

The Collimator

To obtain an image with a gamma camera, it is necessary to project the gamma rays from the source distribution onto the camera detector. The principle of focusing with a lens as in photography cannot be applied in this case since gamma ray photons interact differently from optical photons due to their higher photon energies [20]. The method of absorptive collimation is employed in the case of image formation. The purpose of the collimator is to restrict the gamma rays which reach the crystal to those that are travelling parallel to the lead walls (known as septa) of the collimator. They are designed to absorb gamma rays outside of the narrow solid angle of acceptance. This is an inherently inefficient technique because most of the potentially useful radiation travelling towards the detector is stopped by the collimator.

The design parameters of a collimator are a compromise between resolution and sensitivity. Parallel hole collimators are the most widely used in imaging. The ratio of the intersepta distance and the septa length determines the acceptance angle of the collimator. Septal thickness is chosen to prevent gamma rays from crossing from one hole to the next. The total performance of a collimator depends on the size of the collimator holes, the thickness and the length of the septa, and the source distance.

Fanbeam collimators were designed to be used for brain SPECT studies. It yields better performance in terms of sensitivity and resolution in comparison with parallel hole collimators. The holes of the fanbeam collimators are orientated to converge along the x-axis at a focal line. The holes in the y-direction remain parallel. Due to this focal geometry, the image projection on the crystal is magnified along the x-axis.

The Crystal

The purpose of the crystal is to convert the incoming gamma rays into flashes of visible light. The problem of detecting the photon is now transformed into detecting the flash of light. The most commonly used scintillation crystals in gamma cameras are NaI(Tl). Technical reasons for the usefulness of NaI(Tl) include the following:

NaI(Tl) is a relatively efficient scintillator producing larger impulses with smaller statistical fluctuations that leads to improved energy and spatial resolution

The material is transparent to its own scintillation emissions. If it is not transparent, the flash of light cannot be detected

NaI(Tl) is relatively dense and contains an element of relatively high atomic number, therefore it is a good absorber and efficient detector of penetrating radiations such as x and gamma rays

The output signal provided is proportional in amplitude to the amount of radiation energy absorbed in the crystal.

However, there are also disadvantages:

The NaI(Tl) crystal is quite fragile and easily damaged by mechanical or thermal stresses

Sodium iodide is hygroscopic and therefore encapsulated in a drybox. Exposure to moisture or humidity causes a yellowish discolouration that impairs light transmission

NaI(Tl) crystals of large size are difficult to grow and expensive.

Photomultiplier Tube Array

These are electronic tubes that produce a pulse of electrical current when stimulated by very weak light signals, e.g. the scintillations produced by a gamma ray in a scintillation detector [21].

The inside front surface of the glass entrance window of the PM tube is coated with a photoemissive substance. It ejects electrons when struck by photons of visible light. The photoemissive surface is called the photocathode, and electrons ejected from it are referred to as photoelectrons.

A short distance from the photocathode is a metal plate called the dynode. The dynode is maintained at a positive voltage relative to the photocathode and attracts the photoelectrons ejected from it. A focusing grid directs the photoelectrons toward the dynode. A high speed photoelectron striking the dynode surface ejects several secondary electrons from it. The electron multiplication factor depends on the energy of the photoelectron, which in turn is determined by the voltage difference between the dynode and the photocathode.

Secondary electrons ejected from the first dynode are attracted and accelerated to a second dynode which is maintained at a higher potential than the first dynode. The sequence of acceleration and multiplication is repeated through 10 - 12 additional dynode stages until finally a shower of electrons is collected at the anode. Some manufacturers use Lucite light pipes between the detector and the PM tubes whereas others couple directly to the crystal using optical grease.

Processing Electronics

The processing electronics measures the output signals of the PM tubes. The X and Y signal, generated by the positioning circuitry [7], determines the position of the output. The Z-energy signal is inspected by the pulse height analyser. An output signal is only produced if the gamma ray energy falls within a specified range. The output is transferred as acquisition data used for reconstruction.

2.3 Image Degrading Factors

Image degrading factors of SPECT are responsible for the low image spatial resolution. These factors are

- Collimator blurring
- Attenuation
- Scattering of photons
- Noise in the measured data

2.3.1 Collimator Blurring

The purpose of the collimator is to allow photons from only a limited range of directions to reach the detector. The collimator's spatial resolution is improved by reducing the range of directions of accepted photons. This can be achieved by reducing the collimator-hole diameter or increasing the collimator thickness. However, this strongly reduces the number of photons being detected, resulting in increased noise. To achieve a useful sensitivity, the angular range of photons accepted by each collimator hole cannot be reduced to a single line of integration. This range of directions results in distance-dependent spatial blurring in the acquired projection data which is transposed to the reconstructed images [22].

In other words, collimator blurring is caused by photons not traveling exactly parallel to the collimator hole [23] but still within the solid angle of acceptance of the collimator.

2.3.2 Attenuation

Photons emitted by the radiopharmaceutical will interact with tissue and other materials as they pass through the body by means of Compton scattering and photoelectric interaction [24]. Compton scattering is a photon-electron interaction whereby a photon collides with a free or loosely bound electron, loses part of its energy to the electron and then scatters in a new direction. In the photoelectric effect, a photon is absorbed by an atom and an electron, called a photoelectron, is emitted from an inner orbit of the atom.

Because of these interactions, the number of photons detected differs from the number that would have been detected in a non-absorbing medium. The degree of attenuation is a function of the type of tissue traversed. The attenuation coefficients of a material are a measure of the number of photons removed from the beam, either through photoelectric absorption or through Compton scattering, when traversing the material.

In SPECT, the total linear attenuation coefficient can be written as: Equation Chapter (Next) Section 2

$$\mu = \mu_{photoelectric} + \mu_{Compton} \tag{2.1}$$

where μ is the linear attenuation coefficient, which represents the probability that the photon will undergo an interaction while passing through a unit thickness of tissue.

Stating this simply, μ is a measure of the fraction of primary photons that interact while traversing an absorber and is expressed in units of cm^{-1}.

Let N(a) represent the original number of photons and N(s) represent the number of photons that travel a distance s in a medium. The fraction of photons eliminated over a distance ds is μ(s)N(s). Since the number of photons is decreasing, this can be written as:

$$-dN = \mu(s)N(s) \tag{2.2}$$

If initially N(a) photons are emitted in point s = a along the s-axis, the number of photons N(d) expected to arrive in the detector at position s = d is obtained by integrating (2.2) to produce:

$$N(d) = N(a)e^{-\int_a^d \mu(s)ds} \tag{2.3}$$

In water, the attenuation coefficient of a 140 keV photon is 0.15 cm^{-1} [25]. In a brain with a radius 10 cm, approximately 20 % of the 140 keV photons will be lost due to attenuation.

2.3.3 Scatter Correction

When photons interact with matter they will not only lose energy due to Compton scatter, but will also deflect from their initial pathway. Some of the scattered photons will have a new direction parallel to the hole of the collimator. Although photons lose energy, their energy may still be within the accepted energy range of the detection system. There is no way to distinguish these photons from the primary photons within the energy window.

2.3.4 Poisson Noise

Radioactive decay is a statistical process. The total number of gamma rays emitted per unit time from a radioactive source follows a Poisson distribution. The limited number of detected photons results in a substantial amount of Poisson noise in the projection data.

If the mean number of incident photons per unit area of the detector is denoted by r, then the probability p(n) that there are n incident photons per unit area is given by the general form of the Poisson distribution [26]:

$$p_r(n) = \frac{e^{-r} r^n}{n!} = e^{-r} \frac{r}{1} \frac{r}{2} \frac{r}{3} \cdots \frac{r}{n} \tag{2.4}$$

where ! is the factorial operator.

Individual measurements in a detector system are independent of all others, since each photon results in an independent atomic decay and is detected in only one detector bin.

Due to the statistical nature of photon detection, Poisson noise is one of the factors degrading scintigraphic images, especially at low count levels. Noise reduction is usually achieved by smoothing the projection or reconstructed image using low pass filters. However, this causes additional reduction of the spatial image resolution.

Chapter 3

Image Reconstruction

3.1 Introduction

The basic problem of emission tomography is to reconstruct the three-dimensional distribution of the radioactivity within the patient, given a number of lateral views. This chapter explains how the problem can be overcome and covers the following topics:

3.2 Presentation of the Reconstruction Problem

3.3 The Projection Operator

3.4 The Central Slice Theorem

3.5 Filtered Backprojection

3.6 Iterative Reconstruction

3.7 Ordered Subset Expectation Maximisation (OSEM)

3.2 Presentation of the Problem

The acquisition of data from a gamma camera is represented in Figure 3.1. [27]

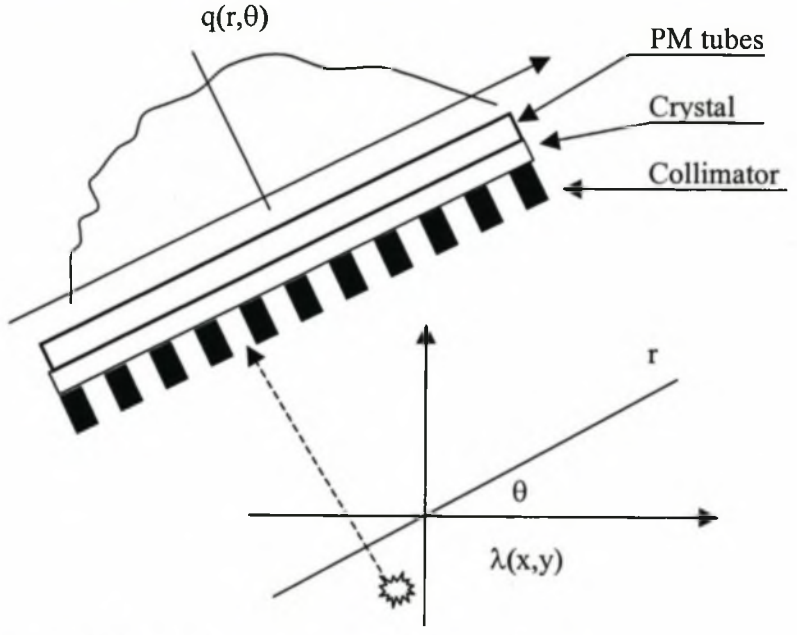

Figure 3.1 Principle of tomographic acquisition.

The detector rotates around the patient. It is assumed that the patient lies along the z-axis. Data is collected at distinct angular positions along projection lines. A projection line is completely specified by its angle and its distance to the centre of the field of view. Reconstruction of this collected data into transverse slices allows one to observe the pattern of emission of the gamma ray photon. From Figure 3.1:

$q(r,\theta)$ can be defined as the number of scintillations detected at any location r along the detector when the head is at angular position θ.

$\lambda(x,y)$ is defined as the estimated number of photons emitted at any point (x,y) in the field of view.

The function q represents the projection of λ onto the crystal. $q(r,\theta)$ is thus the sum of the counts recorded in any time interval at a point r when the detector is at angle θ.

At the end of the acquisition process, each position of the detector contains the number of counts relating to each angular position. Stacking all these projections for varying angles θ results in a two-dimensional (2-D) dataset called a sinogram. A sinogram is a 2-D image that uses r as the column co-ordinate and θ as the row co-ordinate.

In simple terms, the reconstruction problem can be stated as such, "Given the sinogram, q, what is the distribution of radioactivity λ in the slice of interest?"

3.3 The Projection Operator

The collimator defines the geometry of the projection and determines the direction of the incident photon for any scintillation in the crystal. Ideally, the parallel hole collimator allows only photons that are parallel to the axis of its holes to be detected.

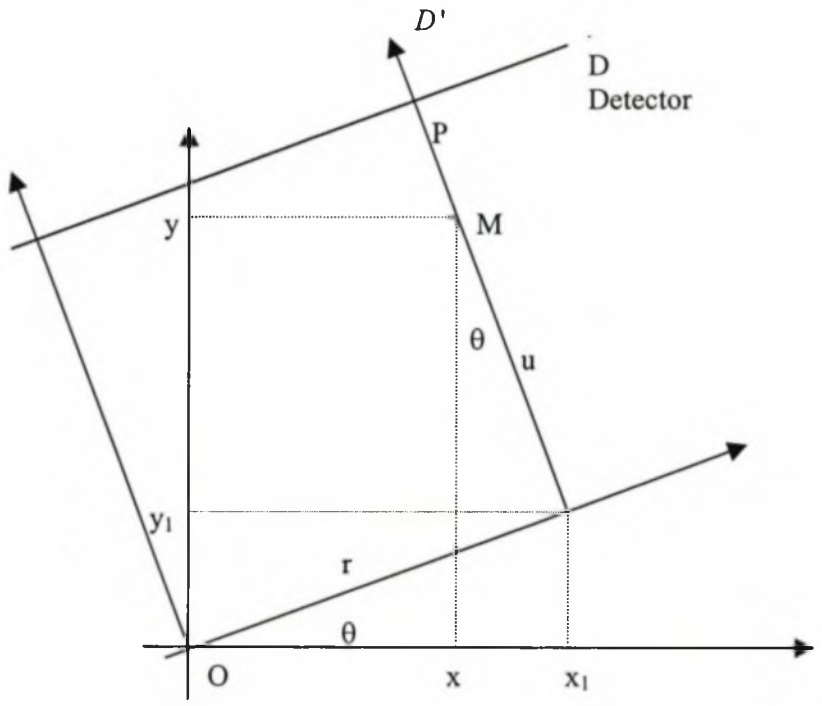

Fig 3.2. Geometry of projection of data onto detector D. Line D' is the set of points M in the field of view that projects perpendicularly on D in P.

Here, the projection is mathematically outlined. To do this, a new co-ordinate system (r, u) is defined by rotating (x,y) over angle θ.

From Figure 3.2 the following is obtained:

$$x_1 = r\cos\theta, \quad y_1 = r\sin\theta$$
$$x_1 - x = u\sin\theta, \quad y_1 - y = u\cos\theta$$

Eliminating x_1 and y_1 Equation Section 3

$$x = r\cos\theta - u\sin\theta \tag{3.1}$$

$$y = r\sin\theta + u\cos\theta \tag{3.2}$$

Rewriting (3.1) and (3.2):

$$r = x\cos\theta + y\sin\theta \tag{3.3}$$

$$u = -x\sin\theta + y\cos\theta \tag{3.4}$$

For each detector angle θ, and for each location r on the detector, the direction of photons is defined by a projection line D', whose equation is given by (3.3) and (3.4). D' perpendicularly projects on D at P.

The projection operation gives the number of counts detected at any point on the detector line as a function of λ(x,y), emitted in any point in the field of view. The ideal case is considered where the projections are continuous, i.e. the projection value is known for every angle and for every distance from the origin. It is further assumed that the projections are unweighted line integrals implying that attenuation, scatter, noise and collimator blurring are excluded.

Mathematically, the transformation of any function λ(x,y) into its parallel beam projections is called the Radon transform and defines the projection operator. The Radon transform q(r, θ) of a function λ(x,y) is the line integral of the values of λ(x,y) along the line inclined at an angle θ from the x-axis at a distance r from the origin.

$$q(r,\theta) = \int_{x,y \in \text{projection line}} \lambda(x,y)\,dx\,dy \tag{3.5}$$

where the projection line is defined by r and θ.

Substituting equations (3.1) and (3.2) in (3.5):

$$q(r,\theta) = \int_{-\infty}^{+\infty} \lambda(r\cos\theta - u\sin\theta, r\sin\theta + u\cos\theta)\,du \tag{3.6}$$

This implies that the value q(r, θ) is the sum of values λ(x,y) along D' where D' is the line of projection. For this reason, q(r, θ) is called the ray-sum. The variable r is the position on the detector, and u defines a location on the line D'

3.4 The Central Slice Theorem

The Central Slice Theorem relates the one-dimensional (1-D) Fourier Transform of the projection q(r, θ) and the 2-D Fourier Transform of the distribution λ(x,y). The theorem is proven for the projection along the y-axis (where θ = 0). The y-axis may be chosen arbitrarily, therefore the theorem holds for any projection angle.

Let $Q(\nu_x,\theta)$ be the 1-D Fourier Transform of q(r,θ).

Since θ = 0, q(r, θ) = q(r,0) = q(x):

$$Q(\nu_x) = \int_{-\infty}^{\infty} q(x) e^{-i2\pi\nu_x x} dx \tag{3.7}$$

where $i = \sqrt{-1}$

Let $\Lambda(\nu_x,\nu_y)$ be the 2-D Fourier Transform of λ(x,y). Then

$$\Lambda(\nu_x,\nu_y) = \int_{-\infty}^{\infty}\int_{-\infty}^{\infty} \lambda(x,y) e^{-i2\pi(\nu_x x+\nu_y y)} dxdy \tag{3.8}$$

Rewriting (3.5):
$$q(x) = \int_{-\infty}^{+\infty} \lambda(x,y) dy \tag{3.9}$$

Substituting (3.9) in (3.7):

$$Q(\nu_x) = \int_{-\infty}^{\infty}\int_{-\infty}^{\infty} \lambda(x,y) e^{-i2\pi\nu_x x} dxdy \tag{3.10}$$

Comparing (3.10) and (3.8), it immediately follows that $\Lambda(\nu_x,0) = Q(\nu_x)$ along the y-axis.

This can be formulated for any angle θ thus:

$$\Lambda(\nu\cos\theta,\nu\sin\theta) = Q(\nu,\theta) \tag{3.11}$$

This can be restated as: the 1-D Fourier Transform of the projections acquired for an angle θ is identical to a central profile along the same angle through the 2-D Fourier Transform of the original distribution.

This means that from the projections over 180° (or 360°) orbit, it is possible to construct the Fourier Transform of the distribution, and the inverse Fourier Transform of the data will give the original distribution.

3.5 Filtered Backprojection

The reconstruction problem can be restated as follows: "Given the sinogram q(r,θ), what is the original function λ(x,y)?". The Fourier-based technique can be used to obtain the distribution but in the discrete case it is less popular because it requires an interpolation step. An alternative procedure can be performed intuitively as follows: For a particular line (r, θ), assign the value q(r, θ) to all points (x,y) along that line. This can be repeated for θ varying from 0 to π The procedure is called "backprojection" and is defined below:

$$\begin{aligned} b(x,y) &= \int_0^{\pi} q(r,\theta)d\theta \\ b(x,y) &= \int_0^{\pi} q(x\cos\theta + y\sin\theta,\theta)d\theta \quad \text{from eq (3.3)} \\ &= \text{backproj}\{q(r,\theta)\} \end{aligned} \tag{3.12}$$

Backprojection represents the accumulation of the ray-sums of all rays that pass through any point (x,y).

Filtered backprojection follows directly from the Fourier Theorem. The inverse Fourier Transform of (3.8) produces:

$$\lambda(x,y) = \int_{-\infty}^{\infty}\int_{-\infty}^{\infty} \Lambda(\nu_x,\nu_y)e^{i2\pi(\nu_x x+\nu_y y)}d\nu_x d\nu_y \tag{3.13}$$

Transforming from rectangular co-ordinates (x,y) to polar co-ordinates (r,θ) results in

$$x = r\cos\theta \text{ and } y = r\sin\theta.$$

Using polar transformation [28] $dv_x dv_y = |v|\,dv d\theta$, where |v| is the absolute value of the Jacobian of the polar transformation and substituting in (3.13):

$$\lambda(x,y) = \int_{-\infty}^{\infty} dv \int_{0}^{\pi} |v|\, d\theta \Lambda(v\cos\theta, v\sin\theta) e^{i2\pi v(x\cos\theta + y\sin\theta)} \tag{3.14}$$

Applying the Central Slice Theorem (3.11) and switching the integrals:

$$\lambda(x,y) = \int_{0}^{\pi} d\theta \int_{-\infty}^{\infty} |v|\, dv Q(v,\theta) e^{i2\pi v(x\cos\theta + y\sin\theta)} \tag{3.15}$$

The definition of backprojection can be applied to (3.15) to yield:

$$\lambda(x,y) = \text{Backproj}\left(\int_{-\infty}^{\infty} |v|\, Q(v,\theta) e^{i2\pi v r} dv \right) \tag{3.16}$$

where $r = x\cos\theta + y\sin\theta$ from equation (3.3).

This shows that the function λ(x,y) can be reconstructed by multiplying $Q(v,\theta)$ by the ramp filter |v| and then backprojecting the inverse of the 1-D Fourier Transform with respect to v. For FBP to be implemented on real data, (3.16) is discretised and 1-D Fourier Transform is replaced by 1-D fast Fourier Transform.

Filtered backprojection is fast and easy to implement but the major limitations are firstly, that the noise distribution is ignored and secondly, that it is difficult to include sophisticated projection models, like attenuation, scatter and collimator blurring.

The method of filtered backprojection suffers the following drawbacks:

- Reconstruction artefacts result from the fact that the actual acquisition differs considerably from the ideal projection model.

- The point spread function is not a Dirac impulse
- The measured projections contain a significant amount of noise.
- Compton scatter contributes significantly to the measurement.

Iterative reconstruction techniques allow some of these effects to be modelled into the algorithm. This is one of the major advantages of iterative methods.

3.6 Iterative Reconstruction

Iterative reconstruction is becoming popular because the algorithm allows easy modelling of the imaging physics such as geometry, attenuation, scatter and noise.

In the discrete case, the elements of the slice are the pixels and each point of measurement on the detector, for each projection angle, is called a bin. The location of a bin is known by its index i and the location of a pixel by its index j. The vector q is the matrix product of matrix C and vector λ. The value λ_i is a weighted sum of the m pixel values in the image therefore:

$$q_i = c_{i1}\lambda_1 + c_{i2}\lambda_2 + \ldots + c_{im}\lambda_m = \sum_{j=1}^{m} c_{ij}\lambda_j \tag{3.17}$$

In matrix notation, (3.17) can be written as:

$$q = C\lambda \tag{3.18}$$

This is the discrete form of the projection operation, where C is the projection operator. The projection operator allows one to find the sinogram given the slice.

Any element of the matrix C, eg c_{ij} can be seen as a weighting factor representing the contribution of pixel j to the number of counts detected in bin i, or the probability that a photon emitted from pixel j is detected in bin i.

The basic idea of iterative reconstruction is to find a solution of vector λ in the equation $q = C\lambda$. The principle is to find the solution by means of successive estimates and not by means of mathematical inversion. The basic sequence of SPECT reconstruction using iterative techniques is as follows:

The algorithm starts with a simple guess as to the nature of the distribution. Next, the projection operator is used to synthesize the projections of the guess through the same number of projections and angles as the acquired data. If the initial guess was correct, then the generated projections would be identical to the measured projections and the algorithm would stop. In general, this is not the case. The difference between the measured and generated projections represents an error. The error is used to generate a correction, which is applied to the guess and completes one iteration of the algorithm. Further iterations of the algorithm generate a new projection and a new correction. When the error between the calculated and measured projections is sufficiently small, the algorithm is said to have converged.

3.6.1 Maximum Likelihood Expectation Maximisation (MLEM)

The most frequently used iterative algorithm in nuclear medicine applications is the MLEM algorithm [26]. It solves a set of linear equations, assuming Poisson noise is present in the projection data. The goal of MLEM is to find a general solution that provides the best estimate of λ in equation (3.18).

3.6.2 Bayes' Theorem

A Bayesian approach to the problem provides an understanding of MLEM. The aim is to seek the most probable solution of the reconstruction Λ given the measured projections, Q. This can be written as p(Λ|Q). Bayes' theorem [29] states that:

$$p(\Lambda \mid Q)p(Q) = p(Q \mid \Lambda)p(\Lambda) \tag{3.19}$$

Rewriting (3.19)

$$p(\Lambda \mid Q) = \frac{p(Q \mid \Lambda)p(\Lambda)}{p(Q)} \tag{3.20}$$

This is Bayes' rule.

- The function p(Λ) is the ***a priori*** probability. This can encompass prior knowledge about the expected reconstruction. It is the likelihood of the image without taking into account the data. For example, if prior information about the anatomy is available from CT or MRI, it can be incorporated into the data [30].

- The function p(Q|Λ) is called the ***likelihood.*** It gives the probability of obtaining measurement Q, assuming that the true distribution is Λ.

- The function p(Λ|Q) is called the ***posterior***. It is the probability of obtaining the reconstruction, or the activity distribution, given the projection data and the prior knowledge.

- The function p(Q) is a ***constant*** value since the projection data Q have been measured and are fixed during the reconstructions.

Maximising the posterior p(Λ|Q) is called the *maximum-a-posteriori* (MAP) approach. The *prior* probability is often assumed to be constant, i.e. it is assumed *a priori* that all possible solutions have the same probability of being correct. This

implies that maximising the *posterior* p(Λ|Q) reduces to maximising the likelihood p(Q|Λ). This is called the maximum likelihood (ML) approach.

It is necessary to compute the likelihood p(Q|Λ) given that the activity or the reconstruction image is available and represents the true distribution. This can be stated differently as: "How likely is it to measure the projection data Q with a SPECT camera, when the true tracer distribution is the reconstructed image Λ?".

3.6.3 The Likelihood Function for Emission Tomography

First consider what one would expect to measure. This can be written in digital form as follows:

$$r_i = \sum_{j=1,J} c_{ij}\lambda_j, \quad i = 1, I \tag{3.21}$$

$\lambda_j \in \Lambda$ is the regional activity present in the volume represented by pixel j.

r_i is the number of photons measured in detector position i.

c_{ij} is a weighting factor and represents the contribution of pixel j to the number of counts detected in bin i, or as the probability that a photon emitted from pixel j is detected in bin i. If the collimation is good, c_{ij} is zero everywhere except for the j that is intersected by the projection line i.

Two values exist for each detector, the expected value r_i and the measured value q_i. The number of photons emitted from m pixels and detected in bin i is a Poisson variable. The likelihood of measuring q_i photons if r_i photons were expected can therefore be determined by equation (2.4).

The history of one photon emission is independent of the other photons. Thus the overall probability is the product of each of the individual ones:

$$\begin{aligned} p(Q|\Lambda) &= p(q_1 \mid r_1).p(q_2 \mid r_2)...p(q_n \mid r_n) \\ &= \prod_i p(q_i \mid r_i) \end{aligned} \tag{3.22}$$

Substituting (3.22) in equation (2.4) yields:

$$p(Q \mid \Lambda) = \prod_i \frac{e^{-r_i} r_i^{q_i}}{q_i!} \tag{3.23}$$

Maximising (3.23) is equivalent to maximising the logarithm, since the logarithm is monotonically increasing. When maximising the log-likelihood, factors not depending on λ_j can be ignored, thus $q_i!$ can be dropped from the equation. The resulting log-likelihood function, written as $L(Q|\Lambda)$, can be determined.

Thus:

$$\begin{aligned} \ln P(Q|\Lambda) &= \ln\left(\prod_i e^{-r_i} r_i^{q_i}\right) \\ &= \sum_i \left(q_i \ln(r_i) - r_i\right) \end{aligned} \tag{3.24}$$

Substituting (3.21) in (3.24):

$$L(Q \mid \Lambda) = \sum_i q_i \ln\left(\sum_j c_{ij}\lambda_j\right) - \sum_j c_{ij}\lambda_j \tag{3.25}$$

Equation (3.25) is called the log-likelihood function. It is of fundamental importance in the MLEM algorithm, because it allows one to take into account the noise characteristics of the dataset.

Maximum Likelihood Expectation Maximisation (MLEM)

To maximise L, it is necessary to compute the first derivative of (3.25), set it to zero and solve for λ as follows:

$$\frac{\partial L}{\partial \lambda} = \sum_i q_i \frac{\partial}{\partial \lambda} \ln\left(\sum_j c_{ij}\lambda_j\right) - \frac{\partial}{\partial \lambda}(c_{ij}\lambda_j)$$
$$= \sum_i c_{ij}\left(\frac{q_i}{\sum_j c_{ij}\lambda_j} - 1\right) = 0, \quad \forall_i = 1, J \tag{3.26}$$

A simple algorithm which guarantees convergence is the expectation maximisation (EM) algorithm.

3.6.4 The Complete Variables

The iterative algorithm described below makes use of the expected value of a Poisson variable that contributes to the measurement. To explain how that value is computed, consider an experiment where two vials containing a known amount of radioactivity are placed in front of a detector. Assume that the efficiency and sensitivity of the detector are known. It is possible to calculate the expected amount of photons that each vial will contribute during a measurement. The expected count is $\bar{a}$ for vial 1 and $\bar{b}$ for vial 2. In an experiment where the two vials are counted simultaneously, and N counts are measured by the detector, the question that arises is "How many photons a and b were emitted by each of the vials?"

A priori, $\bar{a}$ photons from vial 1 and $\bar{b}$ photons from vial 2 would be expected. The detector should then have measured $\bar{a} + \bar{b}$ photons. In general $N \neq \bar{a} + \bar{b}$ because of Poisson noise. The expected value of a, given N is:

$$E(a \mid a + b = N) = \bar{a}\frac{N}{\bar{a} + \bar{b}}$$

and similarly for b.

If more counts were measured than the expected $\bar{a} + \bar{b}$, the expected value is corrected by the same factor. Extension to multiple sources is described below.

The set of "complete" variables are $X = \{x_{ij}\}$, where x_{ij} is the number of photons that have been emitted in pixel j and detected in bin i. The x_{ij}'s are not observable, but if they were known, the observed variables, y_i could be computed.

The expected value of x_{ij} given Λ is:

$$E(x_{ij} \mid \Lambda) = c_{ij}\lambda_j \tag{3.27}$$

From (3.27) the log-likelihood function for the complete variables X can be computed in exactly the same way as it was determined for L.

This results in:

$$L_x(X,\Lambda) = \sum_i \sum_j \left[x_{ij} \ln(c_{ij}\lambda_j) - c_{ij}\lambda_j \right] \tag{3.28}$$

The expectation maximization (EM) algorithm is a two step procedure.

1. Compute the expected value of the function. This can be written as $E(L_x(X,\Lambda)|Q,\Lambda^{old})$. It is not possible to compute $L_x(X,\Lambda)$ since we do not know the values of x_{ij}. However we can calculate its expected value, using the current estimate Λ^{old}. This is called the expectation, or **E- step**.

2. Calculate a new estimate of Λ that maximises the function derived in the first step. This is the maximisation, or **M- step**.

The E Step

The E step yields the following expression:

$$E\left[L_x(X,\Lambda^{old}\,|\,Q,\Lambda^{old})\right]=\sum_i\sum_j\left(n_{ij}\ln(c_{ij}\lambda_j)-c_{ij}\lambda_j\right) \tag{3.29}$$

where

$$\text{where } n_{ij}=c_{ij}\lambda_j^{old}\frac{q_i}{\sum_j c_{ij}\lambda_j^{old}} \tag{3.30}$$

(Equation 3.29) is identical to equation (3.28), except that x_{ij} have been replaced by their expected values n_{ij}.

The M Step

In the M-step, we maximise this expression with respect to λ_j, by setting the partial derivative to zero.

$$\frac{\partial}{\partial\lambda_j}E\left(L_x(X,\Lambda)\,|\,Q,\Lambda^{old}\right)=\sum_i\left(\frac{n_{ij}}{\lambda_j}-c_{ij}\right)=0 \tag{3.31}$$

From (3.31):

$$\lambda_j=\frac{\sum_i n_{ij}}{\sum_i c_{ij}} \tag{3.32}$$

Substitute (3.30) in (3.32) produces the MLEM algorithm:

$$\lambda_j^{new}=\frac{\lambda_j^{old}}{\sum_i c_{ij}}\sum_i c_{ij}\frac{q_i}{\sum_j c_{ij}\lambda_j^{old}} \tag{3.33}$$

Intuitively, (3.33) can be explained as follows:

- The first image $\lambda^{(0)}$ can be a uniform disk enclosed in a field of view, or an image obtained by FBP. The negative values must be set to zero or to small positive values. Since the first image is positive, and because each new value is found by

multiplying the current value by a positive factor, any λ^{new} cannot have negative values and any values set initially to zero will remain zero.

- The EM algorithm can be seen as a set of successive projections/backprojections.

  The factor $\frac{q_i}{\sum_j c_{ij}\lambda_j^{old}}$ is the ratio of the measured counts to the current estimate of the mean counts in bin i. $\sum_i c_{ij}\frac{q_i}{\sum_j c_{ij}\lambda_j^{old}}$ is the backprojection of this ratio for pixel j.

- Equation (3.33), which is to be applied pixel by pixel, can be extended to the whole image and interpreted as:

  $$\text{Image}^{new} = \text{Image}^{old} \text{ X Normalised backprojection of } \left(\frac{\text{Measured projections}}{\text{Projections of image}^{old}}\right)$$

  If the measured and computed sinograms are identical, the entire operation has no effect. If the measured projection values are higher than the computed ones, the reconstruction values tend to increase.

Comparing (3.33) with (3.26) shows that the ML algorithm can be rewritten as:

$$\lambda_j^{new} = \lambda_j + \frac{\lambda_j}{\sum_i c_{ij}}\frac{\partial L}{\partial \lambda_j} \tag{3.34}$$

This shows that the gradient is weighted by the current reconstruction value, which is guaranteed to be positive. This is the iterative scheme of the MLEM algorithm as described by Shepp and Vardi [11] and independently by Lange and Carson [12].

3.7 Ordered Subsets Expectation Maximisation (OSEM)

This technique was proposed by Hudson and Larkin [31] to accelerate the reconstruction process using the MLEM algorithm. With the ordered subset (OS) method, the set of projections is divided into subsets (or blocks). For example, 64 projections divided into 16 subsets will contain 4 images each. An iteration of ordered subsets is defined as a single pass through all the subsets. The subsets are ordered so as to be maximally separated, progressively working through the projections and maintaining maximum distance between the projections in each subset. An important parameter in OS is the choice of subsets. Hudson and Larkin [31] distinguish between:

- **Non-overlapping subsets:** all subsets are mutually exclusive and their union equals the complete set of projection data
- **Cumulative subsets:** every subset is contained within the following subset.
- **Standard:** there is only one subset containing all the projection data; this is equivalent to not using OSEM.

In this study, the following guidelines are used for defining subsets:

- The subsets are non-overlapping
- The number of subsets are decreased as iteration number increases; this helps to promote convergence

Chapter 4

Materials and Methods

4.1 Introduction

Two simulation experiments were formulated to explore the influence of reconstruction and attenuation correction techniques on brain SPECT images. In each experiment a 3-D brain SPECT phantom was created and hypo-perfused lesions with varying contrasts and sizes were added to the digital phantom. Projection data were generated by modelling the effects of Poisson noise, collimator blurring, and attenuation. The projections were reconstructed using filtered backprojection and iterative techniques. Uniform and true attenuation maps were included in the reconstruction algorithm for each technique.

The primary difference between the two experiments related to the construction of the attenuation map. **Experiment I** utilised an attenuation map generated from a PET transmission scan where the attenuation coefficients were downscaled from 511 keV photons to 140 keV photons for typical SPECT radionuclides. This represented the "true" SPECT attenuation map. However, noise from the PET transmission scan was transposed to the SPECT transmission scan. **Experiment II** was designed to produce a more accurate attenuation map and a "true" attenuation map was generated from segmented MRI data. Typical linear attenuation coefficients were assigned to grey matter, white matter, bone, air and fat.

All experiments and analysis were performed using the software package IDL 5.2 (Research Systems, Inc) running on a Pentium III 800MHz system with Redhat Linux 6.2 and also a Sun 450 Model 4300 Workstation.

Both experiments involved the following steps:

4.2 Construction of a brain SPECT software phantom

4.3 Generation of projection data

4.4 Generation of reconstructed data

4.5 Analysis of data

4.2 Construction of a Brain SPECT Software Phantom

The goal was to create a digital representation of the human brain suitable for tomographic image simulation. The steps outlining the construction of the phantom are listed below:

- Acquisition of MRI volume data
- Segmentation of the volume data
- Creation of the activity map
- Creation of the attenuation map
- Manipulation of the phantom

4.2.1 Acquisition of MRI Volume Data

Experiment I

The SPECT software phantom was constructed from segmented MRI data. For this purpose, four high resolution MRI scans were performed on a normal volunteer at the Catholic University of Leuven, Belgium. The scans were

acquired with a Siemens Vision 1.5 Tesla scanner (Erlangen, Germany) using a magnetisation prepared rapid gradient echo sequence (repetition time = 9.7 ms, echo time = 4 ms, inversion = 300 ms, number of excitations = 1, flip angle = 12 degrees, matrix size = 256 X 256, field of view = 256 mm). The volume contained 160 slices; each slice was 256 X 256 with an in-plane pixel size of 1mm x 1mm and a slice thickness of 1mm. The four MRI scans were co-registered to each other using the technique of mutual information [32] and the mean MRI scan was determined. Figure 4.1 shows the lower, central and upper transverse slices of the mean MRI volume.

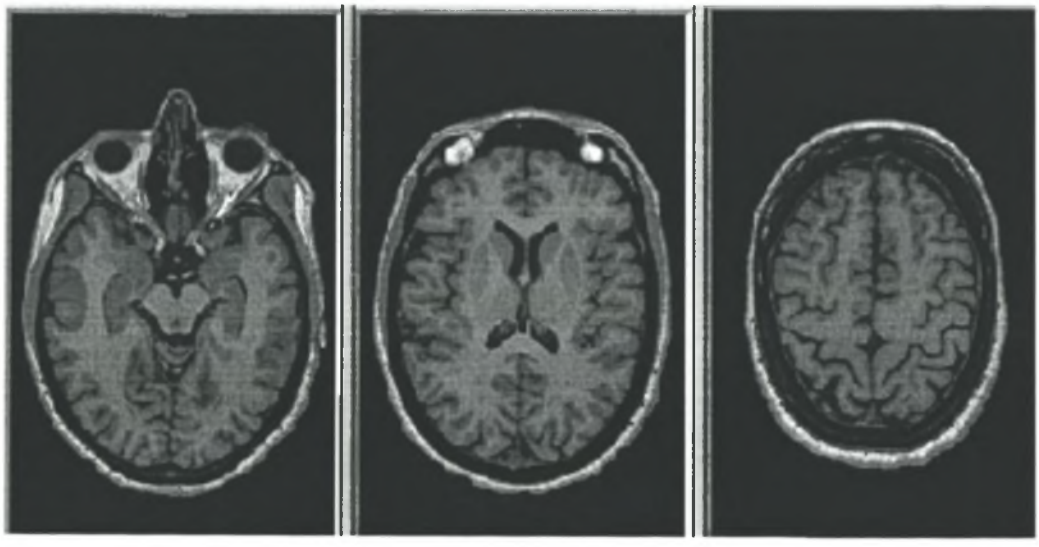

(a) (b) (c)

Fig 4.1 Three transaxial slices of the mean MRI image from which the SPECT phantom was created. (a) lower slice, (b) central slice, (c) upper slice

Experiment II

The second brain phantom was generated from the 3-D digital phantom provided by the BrainWeb database [33]. Construction of the BrainWeb phantom was based on a high resolution (1 mm isotropic voxels), low-noise dataset. The dataset was created by registering 27 scans (T1 weighted gradient

echo acquisitions) of the same individual [34]. The volume contained 181 X 217 X 181 voxels and covered the brain completely, extending from the top of the scalp to the base of the foramen magnum.

4.2.2 Segmentation of the Volume Data

The aim of the segmentation process was to partition the digital image into a set of non-overlapping regions to identify different tissue types or anatomical structures.

Experiment I

Segmentation classified the brain into grey matter, white matter and CSF using Statistical Parametric Mapping version 99 (SPM99) [35]. This classification allowed intensity values to be assigned to each tissue class to obtain a realistic SPECT phantom.

Experiment II

The segmentation of the brain into ten different tissue types was available on the BrainWeb site [33]. The segmentation was performed using first a tissue classifier and then a manual method. Each voxel was assigned a tissue class depending on its tissue type. The tissue types of interest were the grey matter, white matter and CSF (for the activity map) and additionally the fatty tissue, skull and air (for the attenuation map).

4.2.3 Creation of the Activity Map

The segmented MRI volumes for both experiments were assigned relative activity levels. The perfusion ratio of grey matter to white matter was taken as 4:1 [36]. Cerebrospinal fluid (CSF) does not accumulate the radioactive isotope, and therefore

these voxels were assigned a tracer uptake value of zero. A scaling factor was needed to produce realistic values to count levels in the projections. This factor was determined by reviewing the mean values of the projection data of 18 normal HMPAO brain SPECT scans performed at Tygerberg Hospital. The activity map was assigned a scaling factor to produce a similar mean count density of 16 counts per projection pixel in the data of the normal patients.

The generated activity map was reduced to a matrix size of 84 X 84 by eliminating certain sagittal and coronal slices and the number of planes was reduced to 30 for **Experiment I**. The activity map of **Experiment II** used a matrix size of 83 X 83 with 60 planes. This process saved on computational time but maintained the voxel size.

4.2.4 Creation of the Attenuation Map

Experiment I

A PET transmission scan was performed on the same normal volunteer at the Catholic University of Leuven, Belgium. This was acquired on a Siemens-CTI ECAT EXACT HR+ PET scanner using a ^{68}Ge/Ga transmission source. The transmission scan was first co-registered to the mean MRI scan using the method of mutual information [32]. The creation of a true attenuation map required the rescaling of the attenuation coefficients of 511 keV photons of the PET transmission scan to 140 keV, in keeping with ^{99m}Tc-labelled brain compounds. A plot of the linear attenuation coefficients [37] [38] for the different tissue types is displayed in Figure 4.2. A scaling factor of 0.6304 transformed the transmission scan to a realistic attenuation map for a ^{99m}Tc

SPECT scan. This scaling factor verified the results of Zimmerman [39], where a value of 0.6133 was determined as the scaling factor for water.

Type of Tissue	Density (g/cm^3)	μ/ρ (cm^2/g) (150kev)	μ/ρ (cm^2/g) (500keV)	μ (cm^{-1}) (150 keV)	μ (cm^{-1}) (500keV)
A-150 Tissue eq plastic	1.1270000	0.1485	0.09579	0.1673595	0.10795533
Adipose Tissue	0.9500000	0.1500	0.09696	0.14250000	0.092112
Air, dry	0.0012050	0.1356	0.0871	0.000163398	0.00010498
b-100 bone eq plastic	1.4500000	0.1482	0.0923	0.21489	0.1337915
brain, grey/white matter	1.0400000	0.1498	0.0964	0.155792	0.100256
Breast Tissue	1.0200000	0.1493	0.0963	0.152286	0.098226
Lung Tissue	1.0500000	0.149	0.0961	0.156765	0.1008735
Tissue, Soft	1.0600000	0.149	0.0960	0.158152	0.1017388
Bone, Cortical	1.9200000	0.148	0.0902	0.28416	0.1732224

Table 1: Density (ρ) and Linear Attenuation Coefficients (μ) for the different Tissue Types

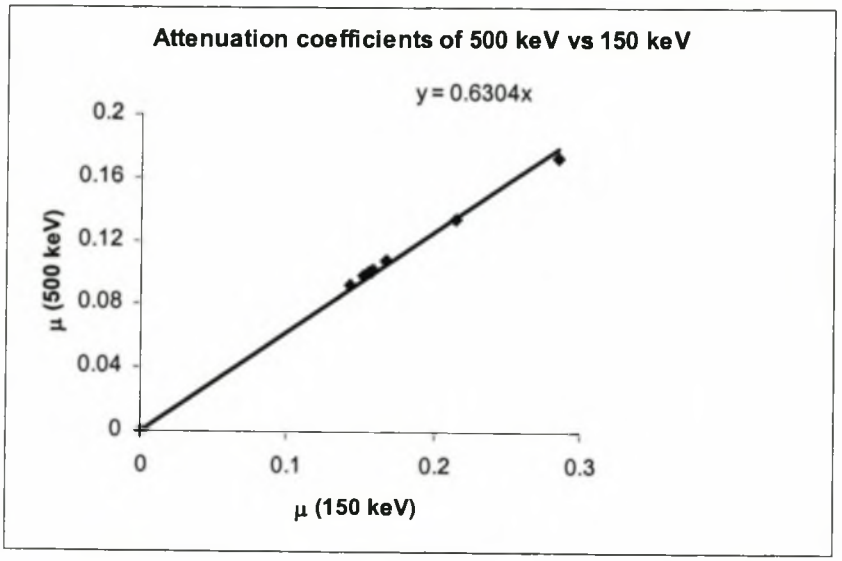

Fig 4.2 Relationship between the linear attenuation coefficients of 500 keV photons versus 150 keV photons.

Experiment II

Appropriate linear attenuation coefficients, obtained from Table 1, were assigned to each voxel of the brain depending on their tissue classifications. Figure 4.3 shows three slices of the image where each grey level corresponds to a particular tissue type. The tissue types of interest utilised in generating the non-uniform attenuation image were the grey matter, white matter, skull, fatty tissue and air. All other voxels in the brain were assigned a linear attenuation coefficient value equivalent to soft tissue. This image was used as the true attenuation map in Experiment II.

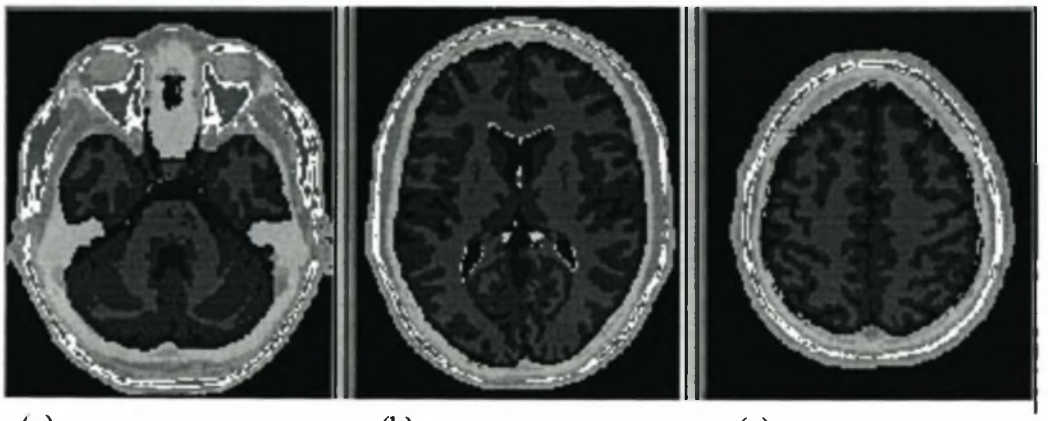

(a) (b) (c)

Fig 4.3. Image from the BrainWeb database from which the attenuation map was derived. Each tissue class is represented by a particular intensity value. (a) lower slice, (b) central slice, (c) upper slice

4.2.5 Manipulation of the Phantom

Seven spherical cold lesions of different contrasts and radii were introduced into the 3-D activity map to represent areas of decreased perfusion. The lesions were positioned at the locations shown in Figure 4.4 for **Experiment I** and Figure 4.5 for **Experiment II**. The number of planes containing the lesions was determined by the pixel size of the lesions.

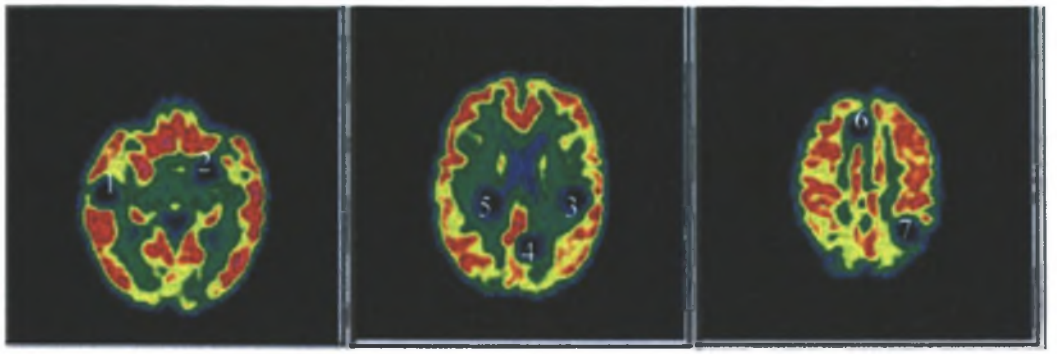

Figure 4.4. Three transaxial slices of the hypo-perfused phantom used in Experiment I. The positions of the seven lesions are indicated.

The lesions were selected to have radii of 5.2 mm and 10.4 mm each, with 50 % and 100 % reduction in intensity. There was no discrimination between white matter and grey matter in the positioning of the cold lesions since certain pathologies can cause reduction in perfusion in both these areas. The phantom with lesions was referred to as the hypo-perfused phantom.

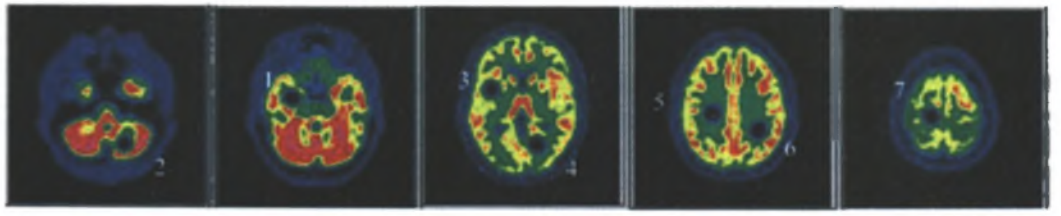

Fig 4.5 Hypo-perfused phantom showing the positions of the 7 lesions. This phantom was used in Experiment II.

4.3 Generation of Projection Data

The SPECT acquisition process was simulated by projecting the baseline and hypo-perfused phantom for 120 angles over 360 degrees with a pixel size of 2.6 mm and detector distance of 12 cm. In this case, the detector distance was the distance from the collimator to the centre of rotation. To ensure that the data were clinically realistic, pseudo-random Poisson noise was added to the data using the pseudo-random generator of IDL 5.2. Each noisy projection data represented a noise

realisation. In both experiments, 100 noise realisations were generated. Detector blurring was also included by means of Gaussian diffusion [22] and attenuation was taken into account.

In the case of the ML methods, the attenuation coefficients were incorporated into the projection and backprojection operations for each iteration. It was programmed by scanning the projection lines in reverse order from the detector towards the patient. While scanning, the attenuation was accumulated by adding the attenuation coefficients of the scanned pixels. The activity could therefore be directly multiplied by the position dependent attenuation. In the case of FBP using Chang's first order attenuation correction, the average attenuation coefficient was computed for each pixel. Thereafter each pixel value of the regular (non-corrected) FBP image was divided by the average attenuation coefficient.

The effects of scatter were excluded in this investigation. The sinogram was smoothed along the detector grid using a 2-D Gaussian kernel with the FWHM equal to 2.6 mm. This was to convolve the ideal projections to compensate for the intrinsic resolution. In order to model the resolution of the system, detector blurring was modelled in the projection using Gaussian diffusion in which the FWHM at a distance d was estimated as:

$$FWHM_d^2 = FWHM_{\text{int}}^2 + (d \text{ X } slope)^2$$

where $FWHM_{int}$ represents the intrinsic resolution

and slope was set to $\frac{0.5}{10}$

4.4 Generation of the Reconstructed Data

Each noisy sinogram was reconstructed using 4 different techniques.

- Filtered backprojection with a calculated uniform attenuation map: FBP-unif
- Filtered backprojection with the true attenuation map: FBP-true
- Maximum likelihood method with a uniform attenuation map: ML-unif
- Maximum likelihood method with the true attenuation map: ML-true

Filtered backprojection was performed using a ramp filter and Chang's first order attenuation correction before any postsmoothing was applied.

The calculated attenuation map was determined as follows: A median filter with a width of 7.8 mm was applied to the sinogram. The zero values were set to 1 and all other values were set to zero. Backprojection and normalisation produced the fraction of projection lines that contained a zero for each of the pixels. Thresholding yielded the object.

An iterative scheme using a decreasing number of subsets was used. For **Experiment I**, the iterative scheme consisted of (iterations X subsets) = (1 X 30, 2 X 24, 3 X 20, 4 X 15, 4 X 12, 4 X 10, 4 X 8, 5 X 6, 5 X 5, 5 X 4, 5 X 3, 5 X 2, 5 X 1). This was approximately equivalent to 423 iterations. The large number of iterations was selected to ensure that the reconstruction approached convergence. In **Experiment II** the number of iterations was reduced to simulate the clinical setting and also shorten the computational time. The (iterations X subsets) were (1 X 30, 1 X 15, 1 X 8, 1 X 4, 1 X 2, 1 X 1). This was equivalent to 60 iterations.

The iterations were carried out on different computers using different operating systems. Experiment I was performed on Pentium III 800MHz system with Redhat Linux 6.2 as the operating system. Each simulation utilised 52 minutes of computer time to perform 423 iterations. Experiment II was run on a Sun 450 Model 4300 Workstation with Solaris 8 as the operating system. The processing time for each simulation required 18 minutes of computer time to perform 60 iterations.

4.5 Analysis of Data

The phantom with lesions allowed an investigation of the performance of the different reconstruction algorithms for the detection of hypo-perfused lesions. Each reconstructed image was postsmoothed, using a 3-D Gaussian blurring kernel. The FWHM of the kernel was varied between zero and 26 mm. Regions of interest, corresponding to twice the lesion size, were positioned over the lesions. It was ensured that the regions did not overlap.

Analysis of the data was performed by comparing the signal to noise ratio (SNR), the root mean squared (rms) bias and rms variance. These figures of merit are discussed below.

4.5.1 Signal to Noise Ratio (SNR)

An important criterion for comparing the performance of a technique is the quality of the images produced. SNR provides an objective measure for evaluating image quality [40]

For notational convenience, the following symbols were used:

B^{nl} represents the reconstructed images of the noiseless SPECT emission data of the baseline phantom, ie the phantom without lesions.

H^{nl} represents reconstructed images of the noiseless hypo-perfused phantom, i.e. the phantom with lesions.

($B_j^{(r)}$) and ($H_j^{(r)}$) represent the values in voxel j of the reconstructed images of noise realisation r of the SPECT emission data of the baseline (B) and hypo-perfused (H) phantoms respectively.

B^{true} and H^{true} denote the "true" baseline and hypo-perfused phantom images respectively.

The response function for each reconstruction technique and for each noise realisation was measured as follows:Equation Section 4

$$s_{nl}(B^{(r)},R)=\sum_{j\in R}(B_j^{nl}-H_j^{nl}).(B_j^{(r)}) \tag{4.1}$$

for the baseline phantom and

$$s_{nl}(H^{(r)},R)=\sum_{j\in R}(B_j^{nl}-H_j^{nl}).(H_j^{(r)}) \tag{4.2}$$

for the hypo-perfused phantom, with R representing a region of interest.

SNR for R was computed using:

$$SNR(R)=\sqrt{2\frac{\left[\bar{s}(B)-\bar{s}(H)\right]^2}{\sigma_s^2(B)+\sigma_s^2(H)}} \tag{4.3}$$

where $\bar{s}$(B) and $\bar{s}$(H) represents the mean of the baseline and hypo-perfused phantom respectively, and σ_s^2(B) and σ_s^2(H) are the variances of $s_{nl}(B^{(r)},R)$ and $s_{nl}(H^{(r)},R)$ respectively over all noise realisations.

4.5.2 Bias and Variance Calculations

The bias and variance measurements were also determined. The bias image was calculated using [41]

$$b(I) = (\bar{I}) - I^{true} \tag{4.4}$$

where $(\bar{I})$ is the mean of ($I^{(r)}$) over all noise realisations and I represents B or H. $\mathbf{I}^{\mathbf{true}}$ represents the "ground truth" image where the "ground truth" image is the SPECT activity map. The root mean squared bias $\tilde{b}(I,R)$ in region R was computed using

$$\tilde{b}(I,R) = \sqrt{\frac{1}{n_R}\sum_{j\in R} b_j^2(I)} \tag{4.5}$$

with n_R the number of voxels in R. The variance image σ^2(I) was calculated using:

$$\sigma^2(I) = \frac{1}{P-1}\sum_{r=1}^{P}\left[(I^{(r)}) - (\bar{I})\right]^2 \tag{4.6}$$

with P equal to the number of noise realisations. The root mean squared standard deviation was computed using:

$$\tilde{\sigma}^2(I,R) = \sqrt{\frac{1}{n_R}\sum_{j\in R}\sigma_j^2(I)} \tag{4.7}$$

4.5.3 Difference between mean image and "ground truth" image

The mean image over all noise realisations using the dataset without lesions was compared to the "ground truth" image. The purpose was to quantify the percentage deviation of the reconstructed image from the "ground truth" image. Two-dimensional regions of interest were drawn at different locations of the brain and the mean difference, which represented the bias, was computed as:

$$\%diff = \frac{mean_{baseline} - mean_{true}}{mean_{true}} \text{ X } 100\% \tag{4.8}$$

Two-dimensional regions were selected to represent the scenario of a normal clinical setting where, typically, regions over a particular area are drawn and the counts obtained. This method provided a simple measure of the bias contained in these counts.

Chapter 5

Results

5.1 Introduction

The results of the two experiments are presented independently in the following sequence:

- Phantoms
- Reconstructions
- Signal to Noise Ratio
- Bias and Variance

5.2 Experiment I

In Experiment I, only 30 planes of the 3-D volume data were utilised. This was to reduce the computation time for the reconstructions. The sagittal view displayed in Fig 5.1 shows the three slices of all images presented for Experiment I. A lower, central and upper portion of the brain is depicted.

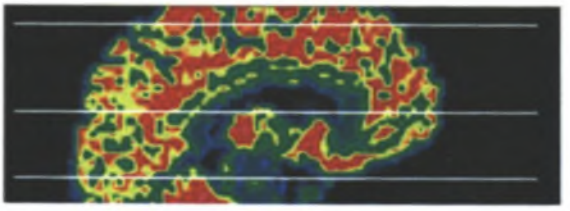

Fig 5.1. A sagittal slice indicating the three planes of the images that are displayed.

5.2.1 Phantoms

5.2.1.1 Activity Map

Three transaxial views of the activity are presented in Figure 5.2. The phantom was constructed from a high resolution MRI image. The intensity of grey matter to white matter was assigned in the ratio of 4:1 with cerebrospinal fluid set to a value of zero.

For visualisation purposes, the images have been postsmoothed with a 3-D Gaussian kernel of 2.6 mm. This represented the "ground truth" image. All projections pertaining to Experiment I were generated from this activity map.

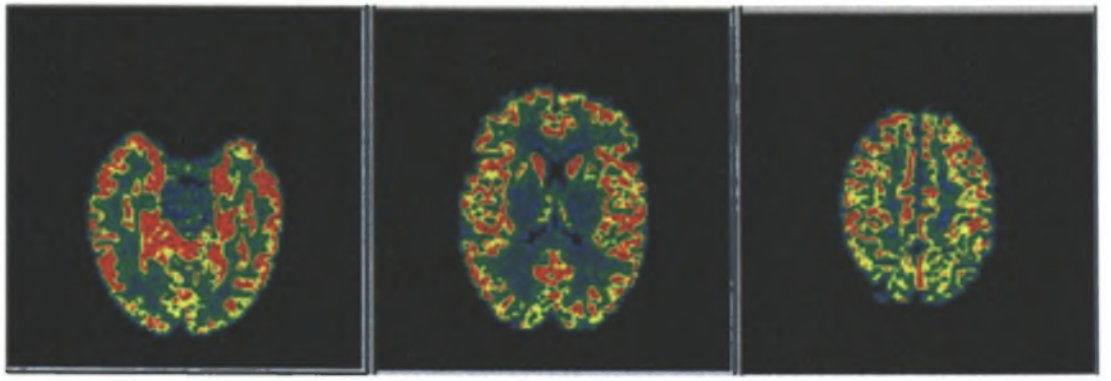

Fig 5.2. Three slices of the SPECT activity map representing the "ground truth" image

5.2.1.2 Attenuation Maps

Three transaxial slices of the "true" attenuation map used in Experiment I are shown in Figure 5.3. The attenuation map was derived from a PET transmission scan performed on the same patient. The original PET transmission scan contained noise and this was transformed as non-uniformities in the attenuation coefficients. This can be observed from the profile drawn through the central slice of the attenuation map and presented in Figure 5.4. No smoothing was performed on the attenuation maps. The "true" attenuation map was used to generate the projection data.

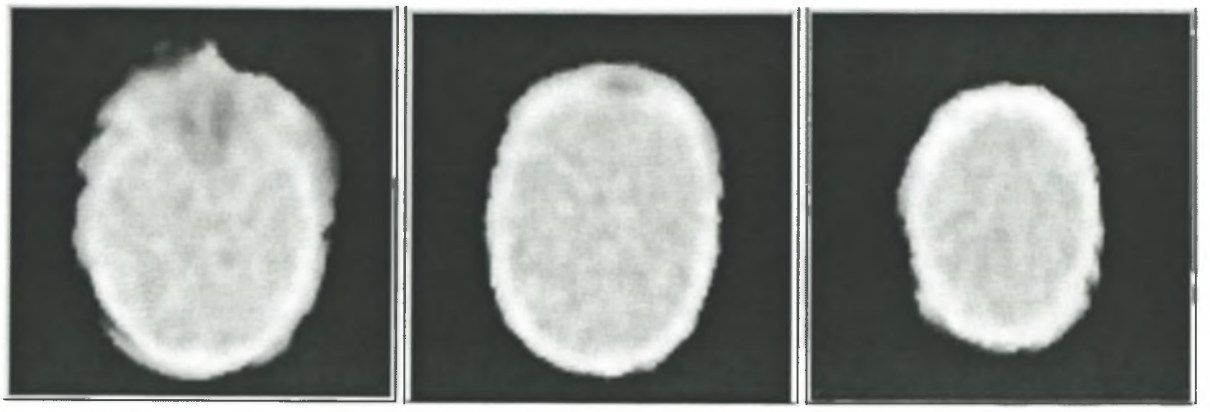

Fig 5.3. Three transaxial slices of the attenuation map transformed from the PET transmission scan. This is used as the "true" attenuation map in Experiment I

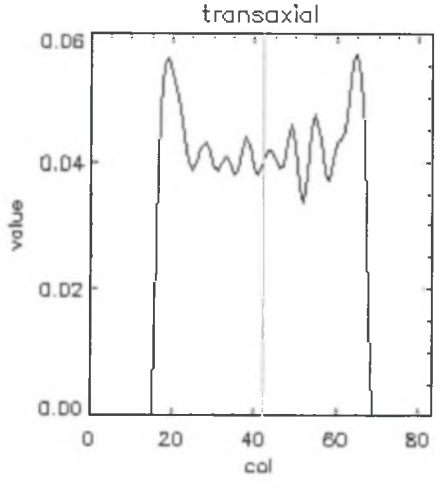

Fig 5.4. Profile through the "true" attenuation map shown. The y-axis shows the value of the attenuation coefficients as pixel^{-1} where 1 pixel = 2.6 mm. The x-axis is along the profile line.

5.2.3 Reconstructions

Three transaxial slices of a single dataset were reconstructed with the four different reconstruction algorithms and presented in Figure 5.5 (a) – (d). Gaussian smoothing of 2.6 mm was applied to the images. The displayed images show lesion sizes with a radius of 10.4 mm and 100 % reduction in intensity. It can be observed that the reconstructions performed with the iterative technique are still rather noisy when compared to the filtered backprojection method.

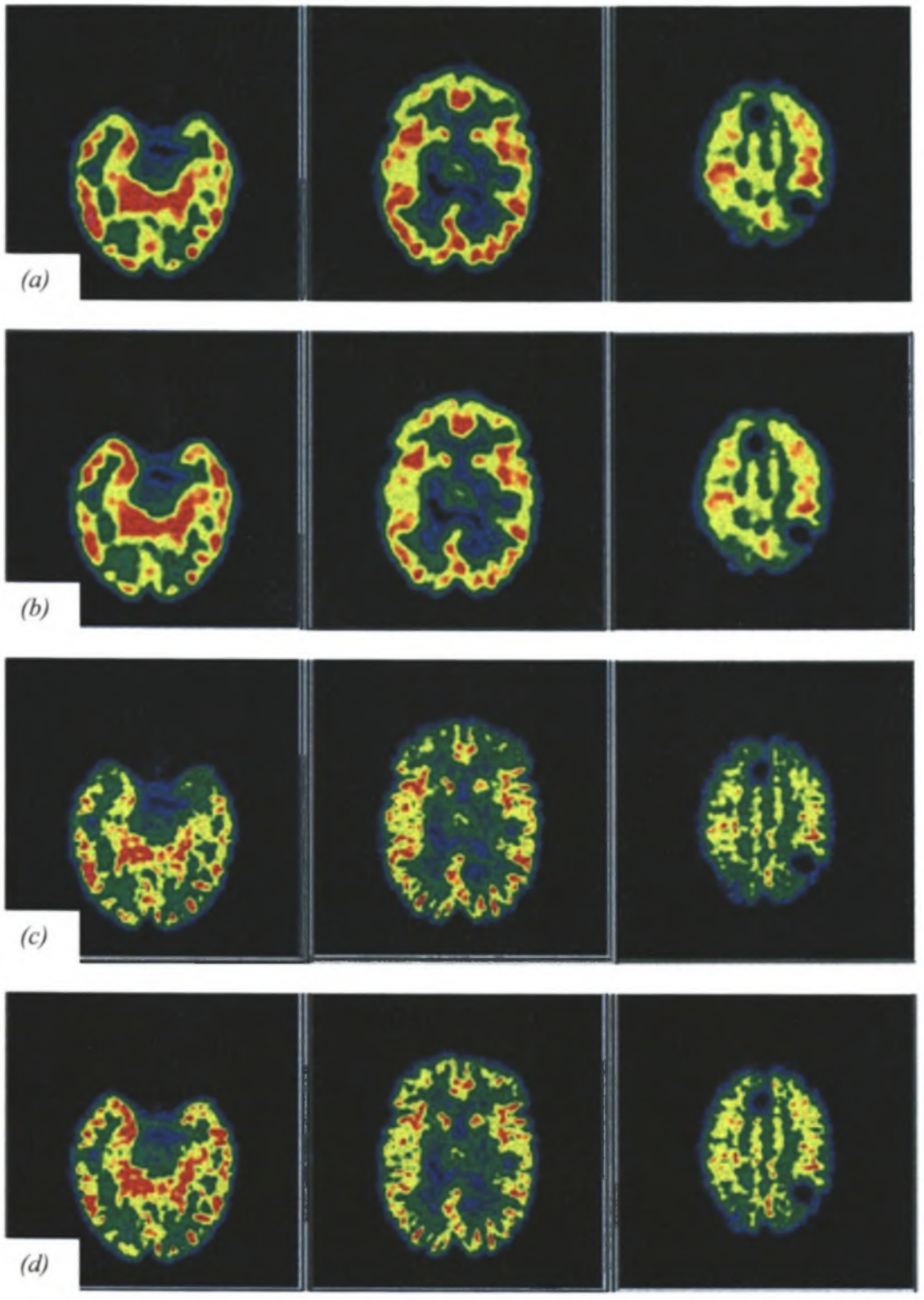

Fig 5.5 (a) – (d). Four sets of noisy reconstructions using the different reconstruction methods. (a) FBP-unif, (b) FBP-true, (c) ML-unif, (d) ML-true. Gaussian smoothing with kernel of 1 pixel was performed.

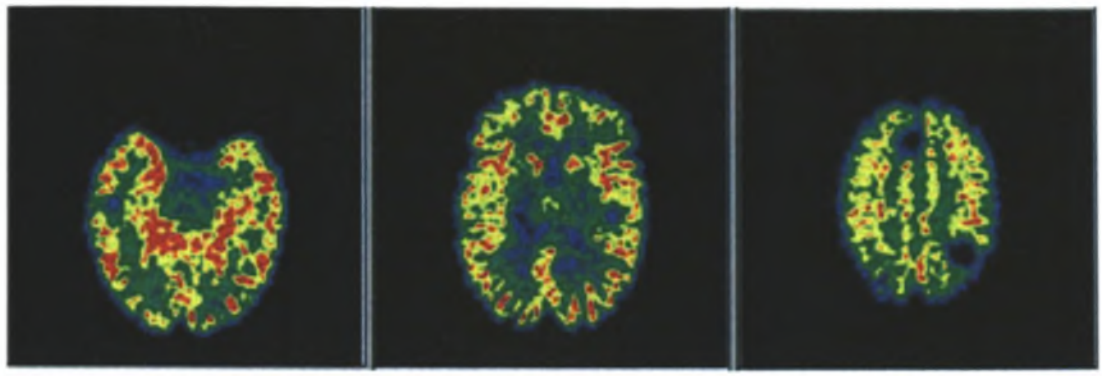

(a)

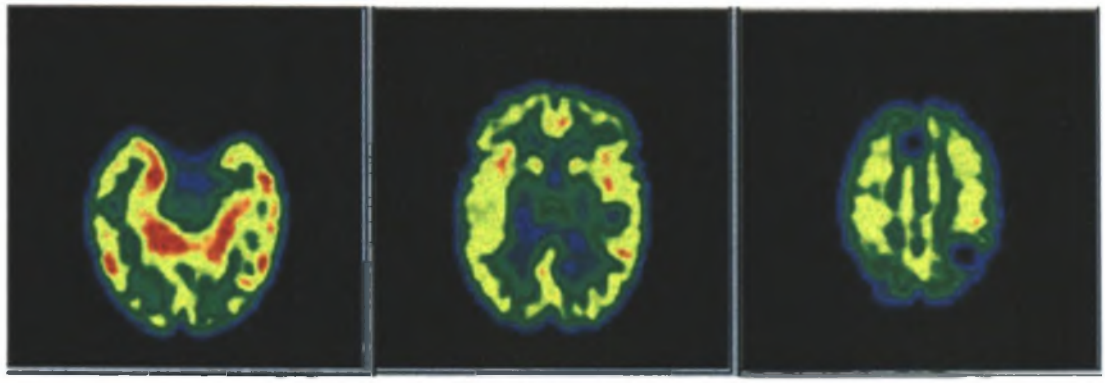

(b)

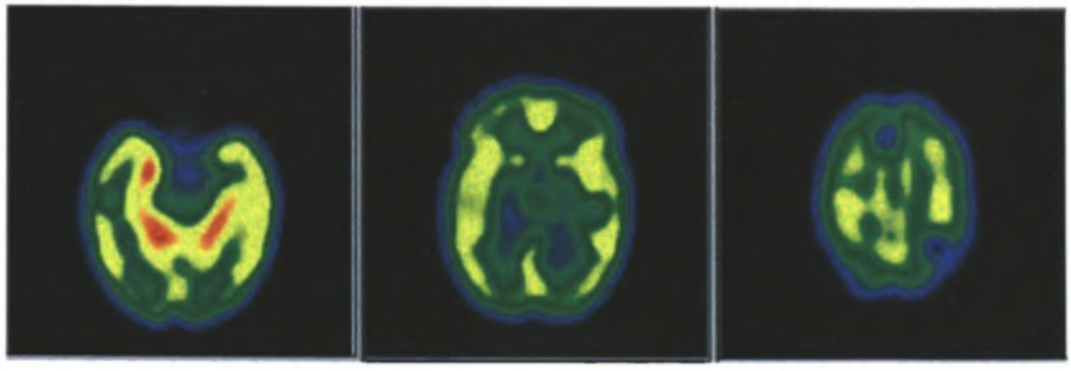

(c)

Fig 5.6 Noisy ML-true reconstructions with different Gaussian smoothing kernels (a) no smoothing, (b) smoothing of 5.2 mm (c) smoothing of 10.4 mm

The influence of postsmoothing on the images is shown in Figure 5.6. Reconstructions using the ML-true method are displayed with varying postsmooth values of 0, 5.2 mm and 10.4 mm corresponding to Gaussian kernels of 0, 2 and 4 pixels retrospectively. The noise in the images is worse in the absence of smoothing. However, smoothing reduces the noise, but the resolution deteriorates.

5.2.4 Signal to Noise Ratio (SNR)

Signal to noise ratios were computed from equation 4.3 for the different reconstruction algorithms. These values are plotted as a function of smoothing with a 3-D Gaussian kernel and displayed in Figures 5.7 and 5.8. Figure 5.7 shows the curves for 100 % reduction in intensity and lesion size equal to 5.2 mm. The lesion size in Figure 5.8 is equal to 10.4 mm with 100 % reduction in intensity. The postsmoothing in the curve is expressed as pixels where 1 pixel = 2.6 mm. Figure 5.7 illustrates that postsmoothing of between 2 and 4 pixels produce the best SNR in most regions of the brain. The ML reconstruction method with the true attenuation map performs best. The other reconstruction methods demonstrate very little difference in performance. The curves of SNR versus postsmooth for the other datasets demonstrated a similar pattern and are not shown here.

5.2.5 Bias and Variance

Figure 5.9 shows the rms standard deviation as a function of the rms bias in the image. It is observed that the standard deviation decreases with postsmoothing at the expense of increased bias. It is also clear from the bias - standard deviation curves that the ML methods perform best when some postsmooth is applied (between 2 and 4 pixels corresponding to 5.2 and 10.4 mm).

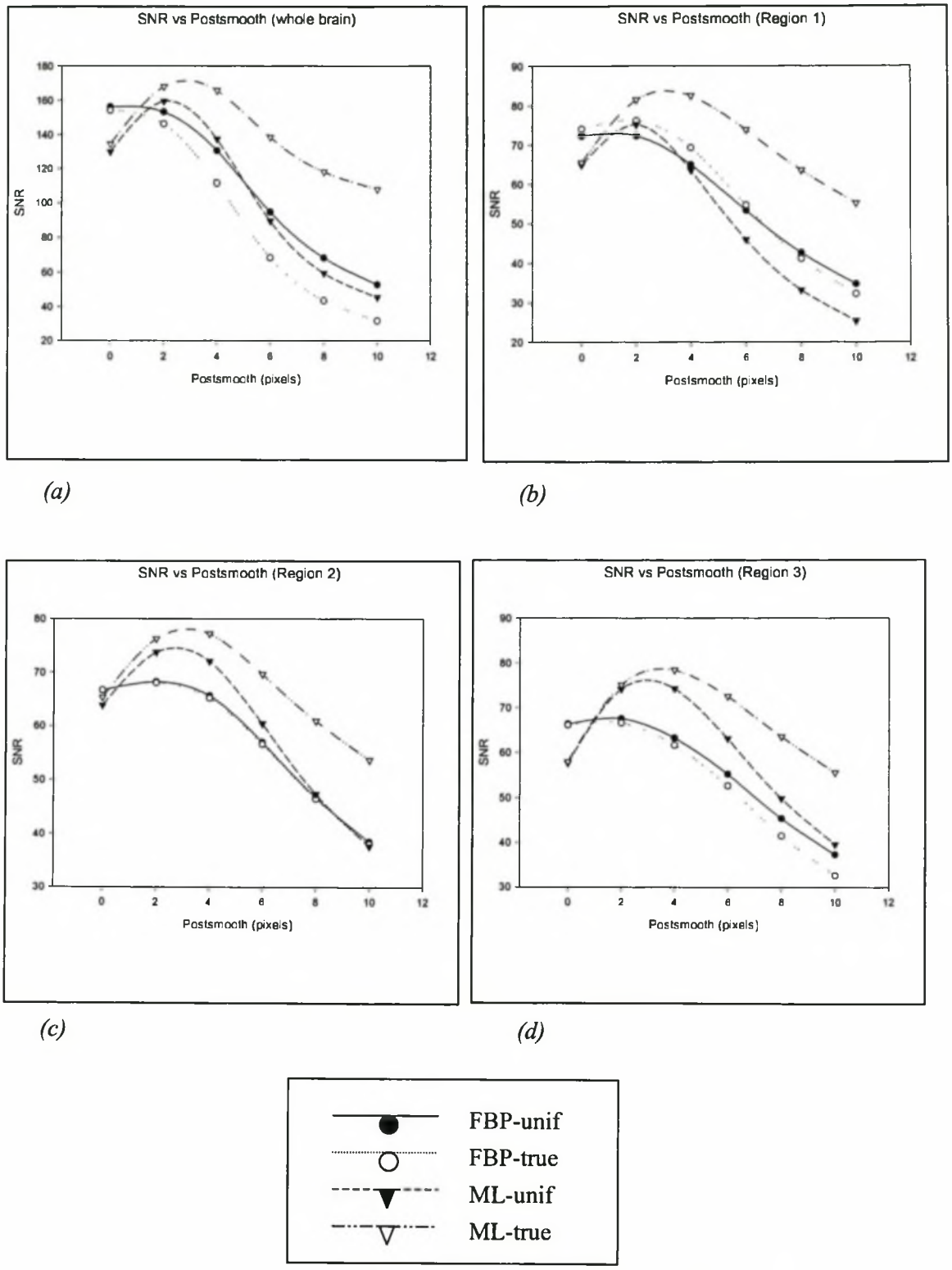

Fig 5.7 (a) – (d) Plots of SNR vs postsmooth for the different regions of the brain for the dataset corresponding to 100 % reduction in intensity and lesion size = 5.2 mm in radius.

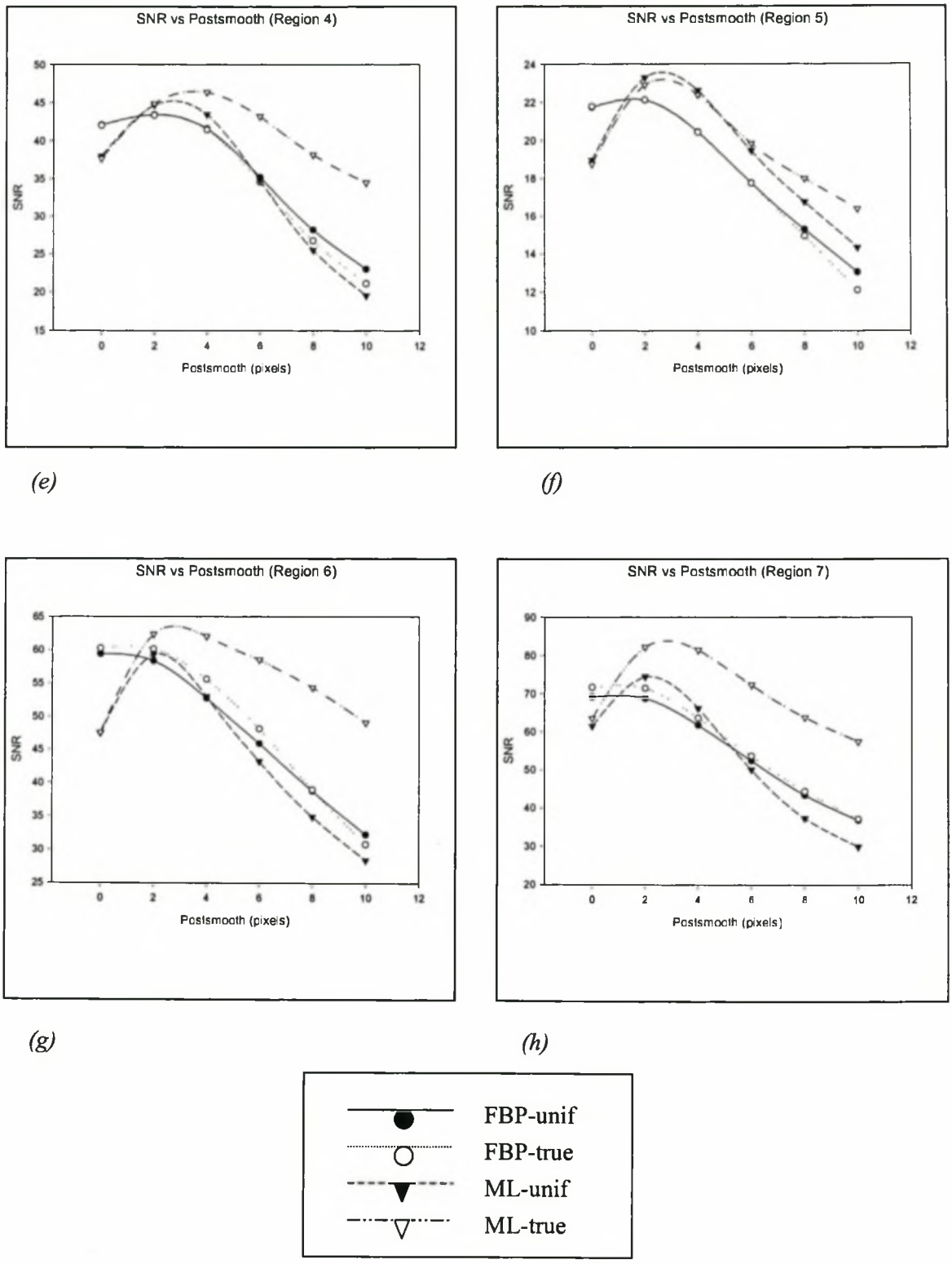

Fig 5.7 (e) – (h) Plots of SNR vs postsmooth for the different regions of the brain for the data set corresponding to 100 % reduction in intensity and lesion radius = 5 2 mm.

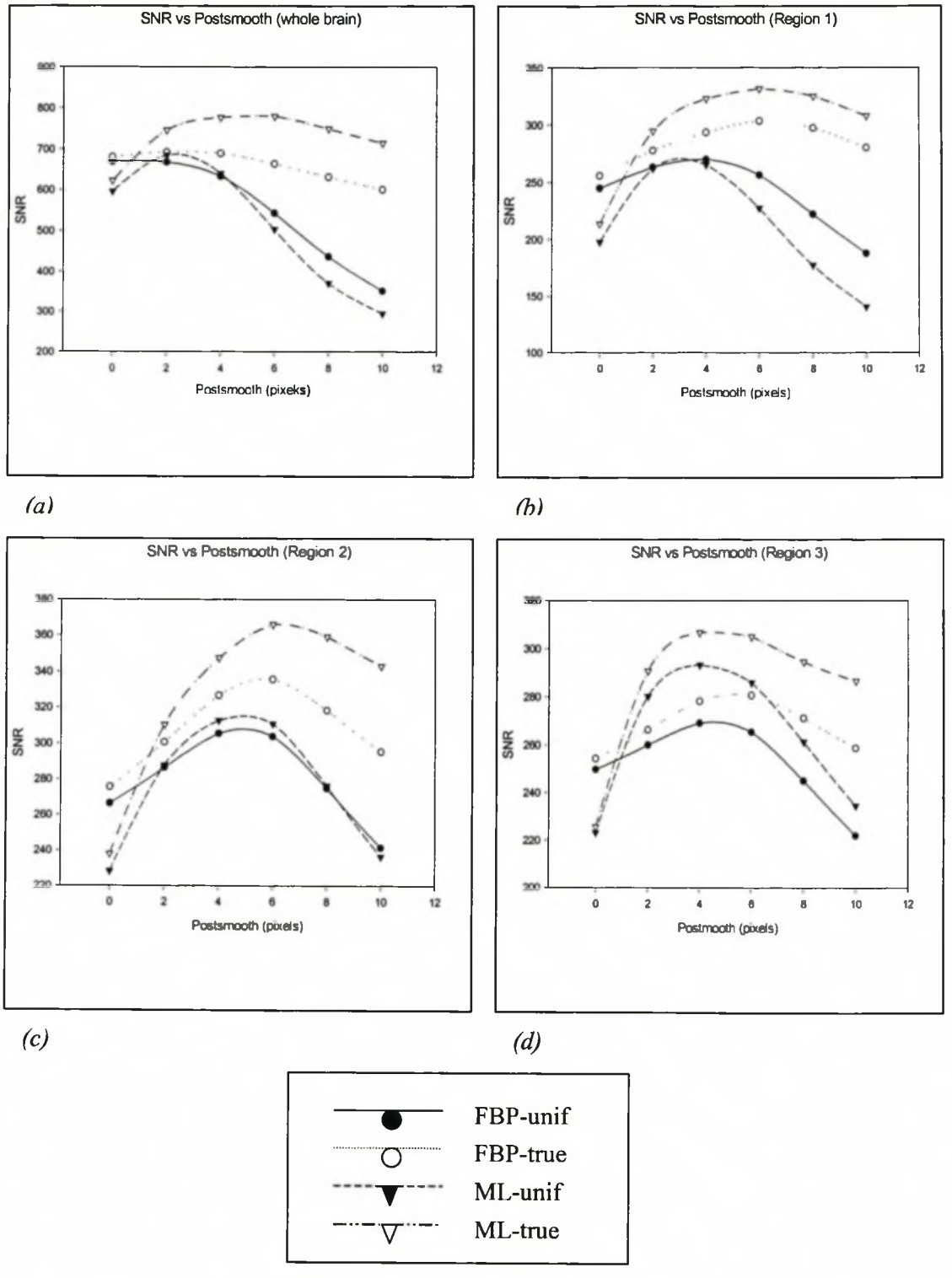

Fig 5.8 (a) – (d) Plot of SNR as a function of postsmooth for the dataset corresponding to 100 % reduction in intensity and lesion radius = 10.4 mm.

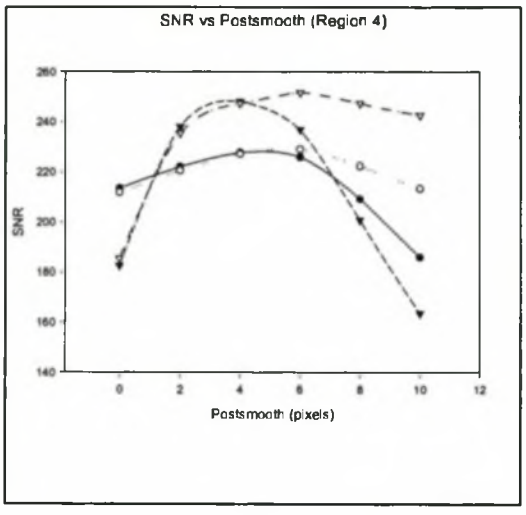

(e)

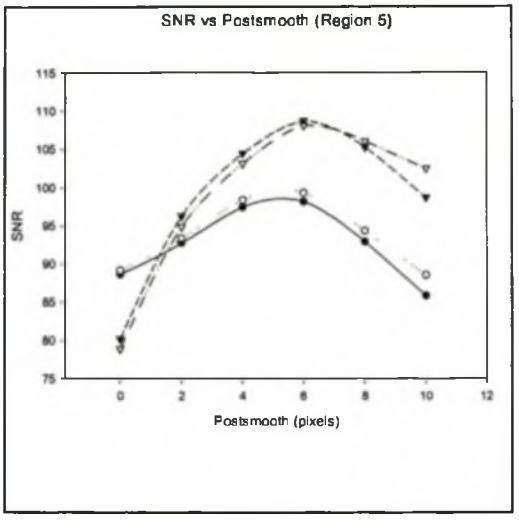

(f)

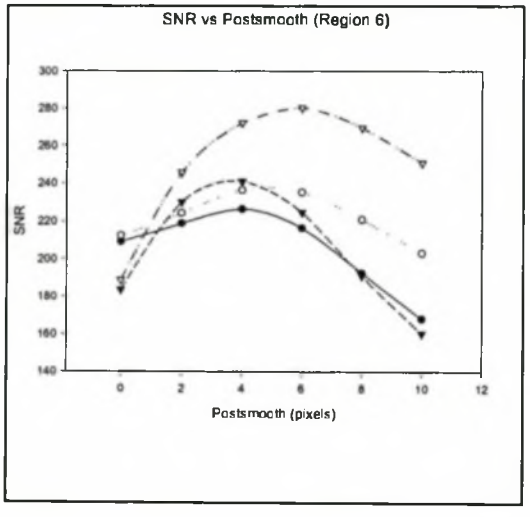

(g)

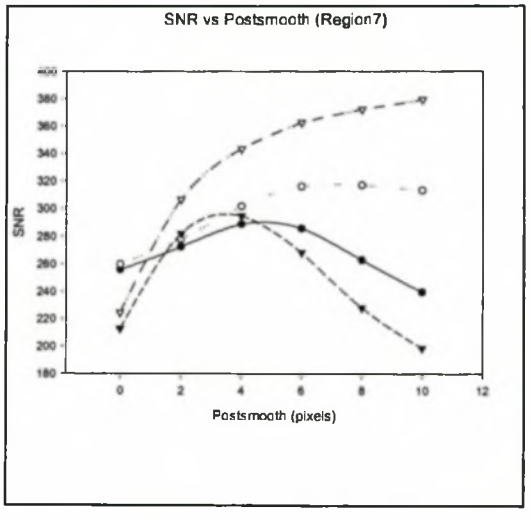

(h)

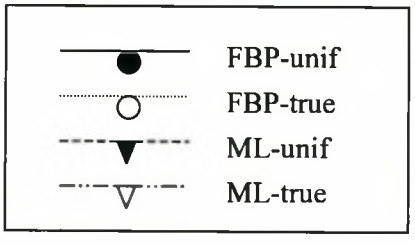

Fig 5.8 (e) – (h) Plot of SNR as a function of postsmooth for dataset corresponding to 100 % reduction in intensity and lesion radius = 10.4 mm.

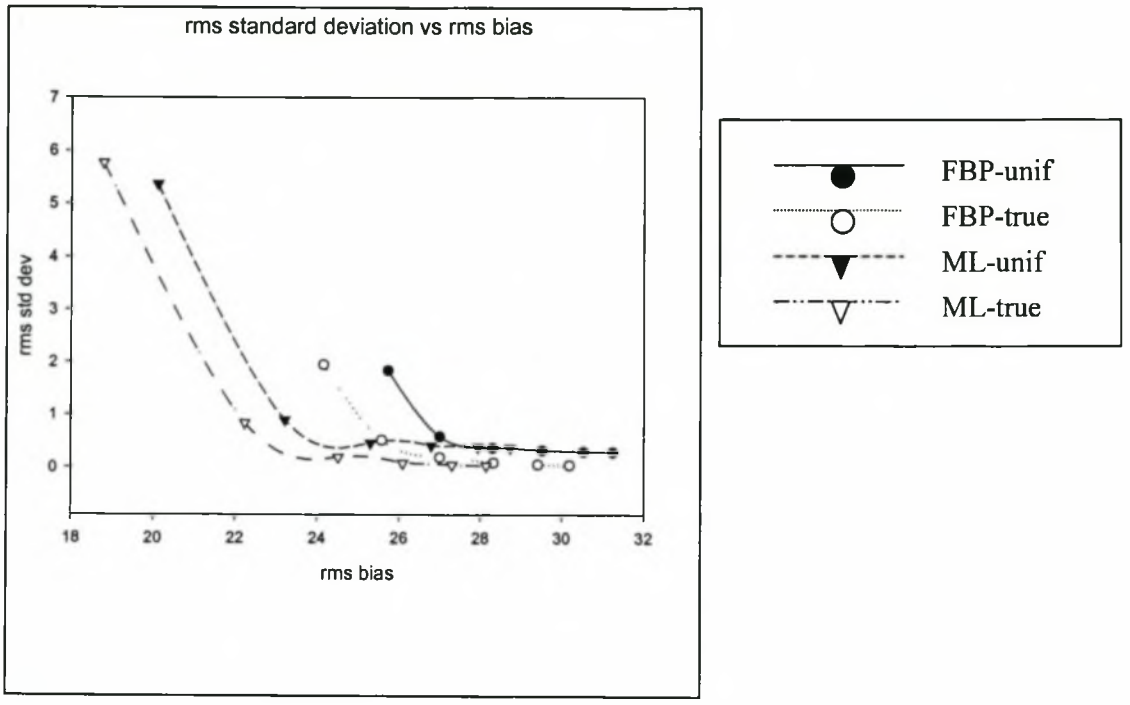

Fig 5.9 Plot of rms standard deviation versus rms bias of the whole brain. The points on the curve indicate a postsmooth of 0, 2, 4, 6, 8 and 10 pixels.

5.3 Experiment II

5.3.1 The Baseline and Hypo-Perfused Phantoms

The entire 3-D volume data, consisting of 60 planes, was used in Experiment II. The sagittal slice, displayed in Figure 5.10, shows the three slices of the brain that are presented for Experiment II.

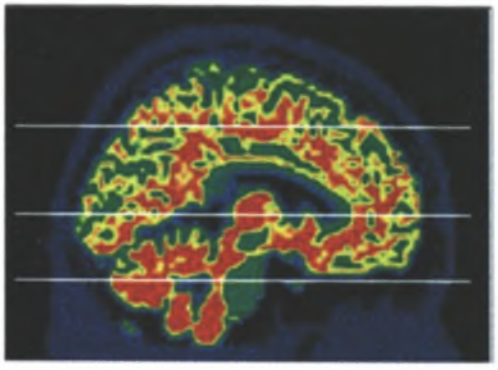

Fig 5.10 Sagittal slice indicating the three planes of the images that are displayed

The SPECT activity map is shown in the Figure 5.11. The phantom displays a high resolution SPECT brain where sufficient detail of the internal structures are observed. For Experiment II, this represented the "ground truth" image.

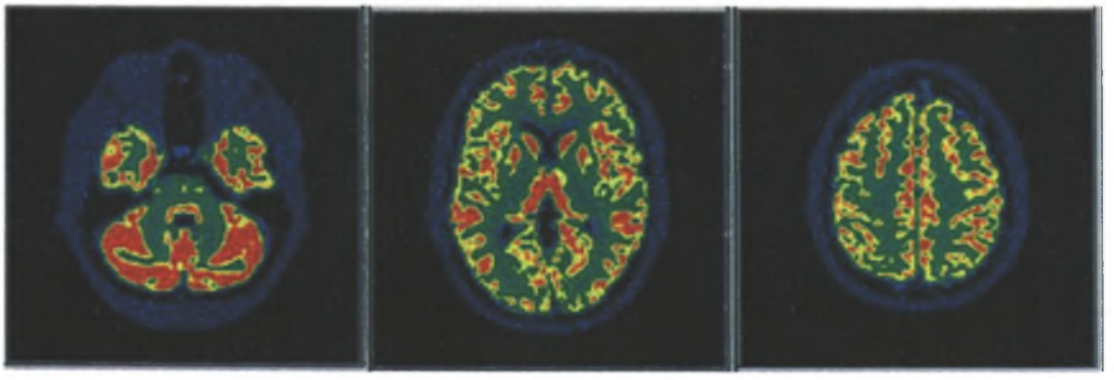

Figure 5.11 The SPECT activity map used as the "ground truth" image in Experiment II

5.3.2 Attenuation Maps

Three slices of the "true" attenuation map are displayed in Figure 5.12. This attenuation image was determined from the segmented MRI images. The linear attenuation coefficients for the different tissues were assigned as per Table 4.1. It is observed that bony structures have higher attenuation coefficients (represented by white areas) when compared to grey and white matter regions of the brain.

An example of a uniform attenuation map is shown in Figure 5.13. An attenuation coefficient of 0.15 cm^{-1} was used.

Fig 5.12 True attenuation map determined from the segmented MRI image

Fig 5.13 Uniform attenuation map determined from the projection data with linear attenuation coefficient of 0.15 cm^{-1}

5.3.3 Reconstructions

Images reconstructed with the four different algorithms are presented in Figure 5.14 (a) – (d). The FBP images were postsmoothed with a 3-D Gaussian kernel of 2.6 mm, equivalent to 1 pixel. A smoothing kernel of 5.2 mm, equivalent to 2 pixels, was used for the ML images. These smoothing parameters were selected purely for display purposes.

Relative to Experiment I, the amount of Poisson noise was increased in Experiment II to simulate realistic patient acquisition data. This required additional smoothing. The displayed images were created from the dataset with 100 % reduction in intensity and lesion radius of 10.4 mm.

The effect of smoothing on the images is shown in Figure 5.15. The displayed images were postsmoothed with a kernel size of 0, 5.2 mm and 10.4 mm respectively, corresponding to 0, 2 and 4 pixels. Figure 5.15 demonstrates that smoothing reduces the noise in the image, but the resolution is worsened. This is validated by the fact that certain structures of the brain, for example the caudate nucleus (indicated by the arrows), is clearly seen with a smoothing of 5.2 mm but cannot be distinguished when the smoothing is increased to 10.4 mm.

5.3.4 Signal to Noise Ratio

Signal to noise ratios were determined for the different reconstruction algorithms. These values are plotted in Figures 5.16 (for a lesion size of radius 5.2 mm) and Figure 5.17 (lesion radius = 10.4 mm). The x-axis of the curve represents the postsmoothing expressed in pixels where 1 pixel = 2.6 mm.

Figure 5.16 demonstrates that the performance of the ML reconstruction methods is superior to the FBP methods. Another observation is that SNR peaks at a smoothing of 4 pixels (10.4 mm) and then decreases.

The curves for lesion size of 4 pixels (10.4 mm) are presented in Figure 5.17. Regions 2, 4 and 7 exhibit a pattern where the SNR increases until a smoothing of 4 pixels (10.4 mm), and then decreases. The other regions demonstrate a local peak at a smoothing of 4 pixels (10.4 mm), a slight decrease, and then a progressive increase in SNR. The curves for regions 1, 3, 5 and 6 of Figure 5.17 display this pattern explicitly.

In both datasets, the ML methods of reconstruction demonstrate higher SNR values when compared to the FBP methods. However, very little differences in SNR can be observed between the true and the uniform attenuation maps. An attempt was made to quantify these differences using equation (5.1) for each region and for each postsmooth. Equation Section 5

$$\%\Delta = \frac{N_{unif} - N_{true}}{N_{true}} \text{ X } 100\% \tag{5.1}$$

where N refers to either FBP or ML method of reconstruction.

The maximum difference between FBP-unif and FBP-true was 2.3% and between ML-unif and ML-true was 4.9%. These values were observed for a postsmooth of 10 pixels (26 mm). In the range of smoothing of 2 and 4 pixels (5.2 mm and 10.4 mm), the maximum difference was computed to be 1.5 % for FBP and 1.7 % for ML.

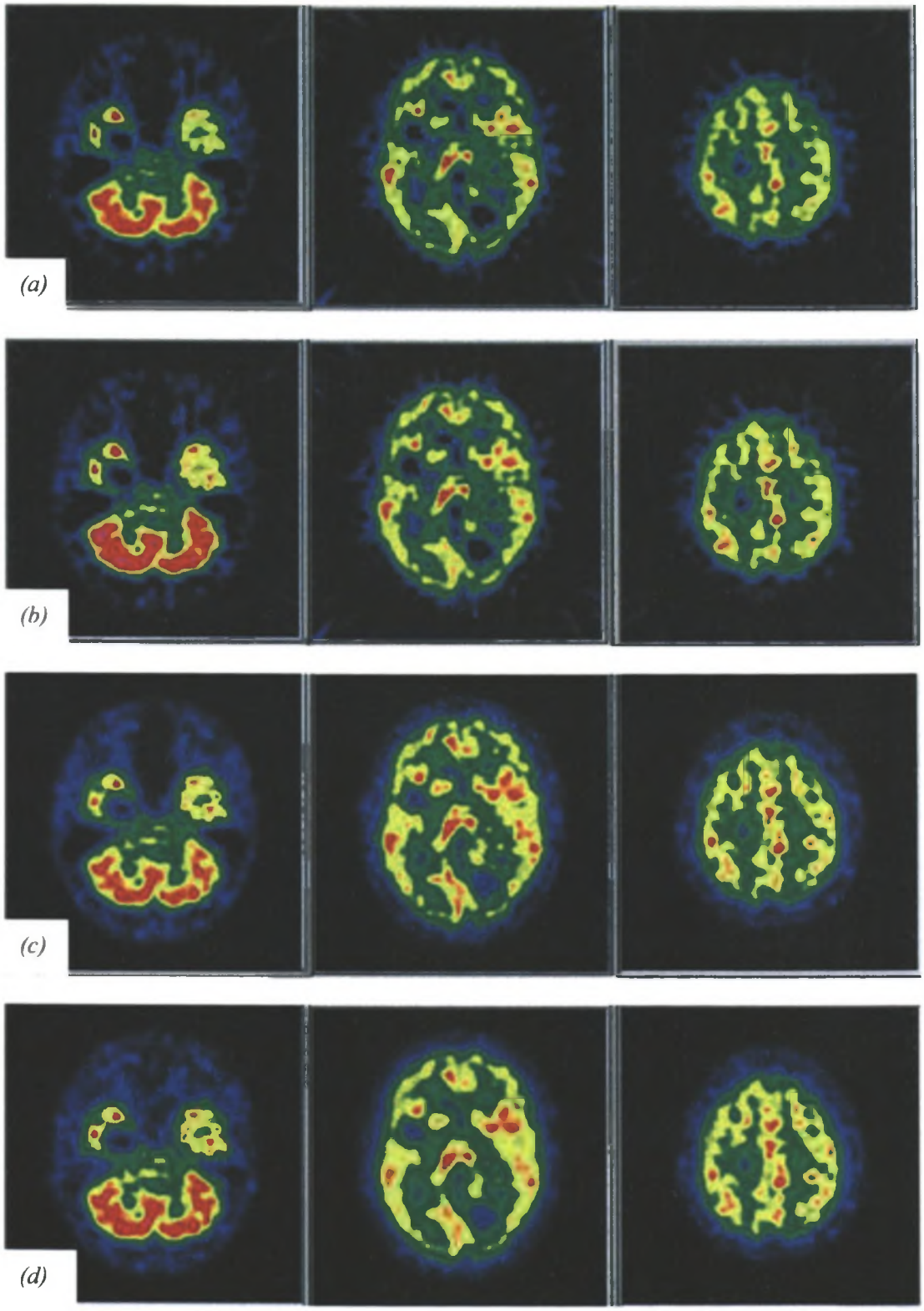

Figure 5.14 Images reconstructed from a noisy sinogram with the four different reconstruction algorithms. (a) FBP-unif (b) FBP –true (c) ML-unif (d) ML-true

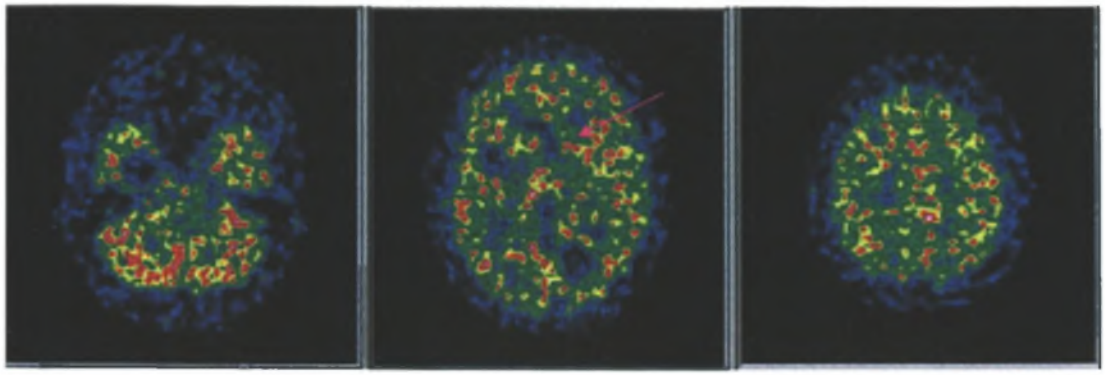

(a)

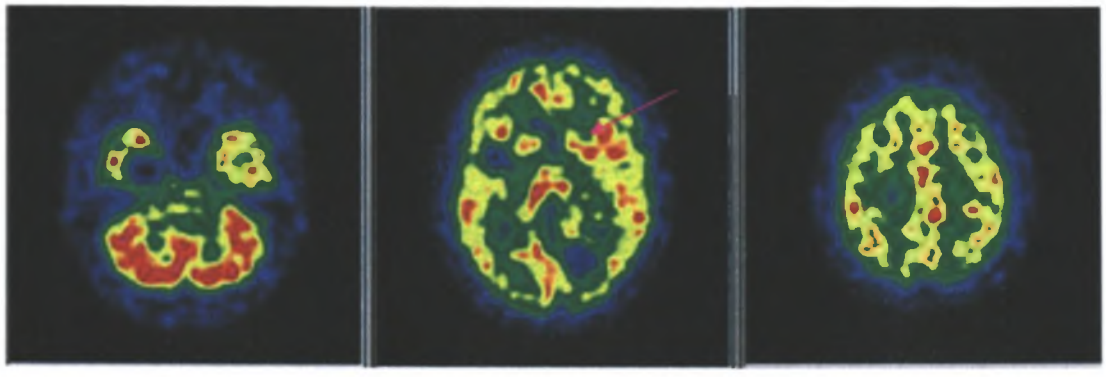

(b)

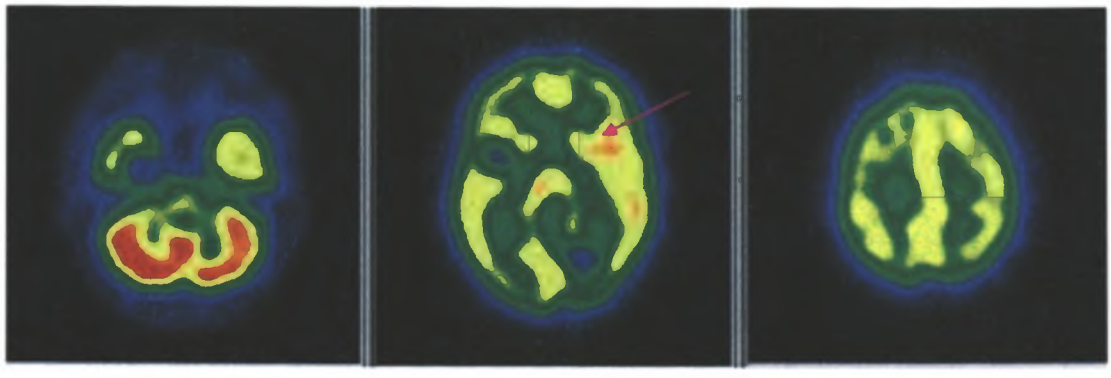

(c)

Fig 5.15 The effects of postsmoothing on ML-true reconstructions are displayed. (a) postsmooth = 0 (b) postsmooth =5.2 mm (c) postsmooth = 10.4 mm

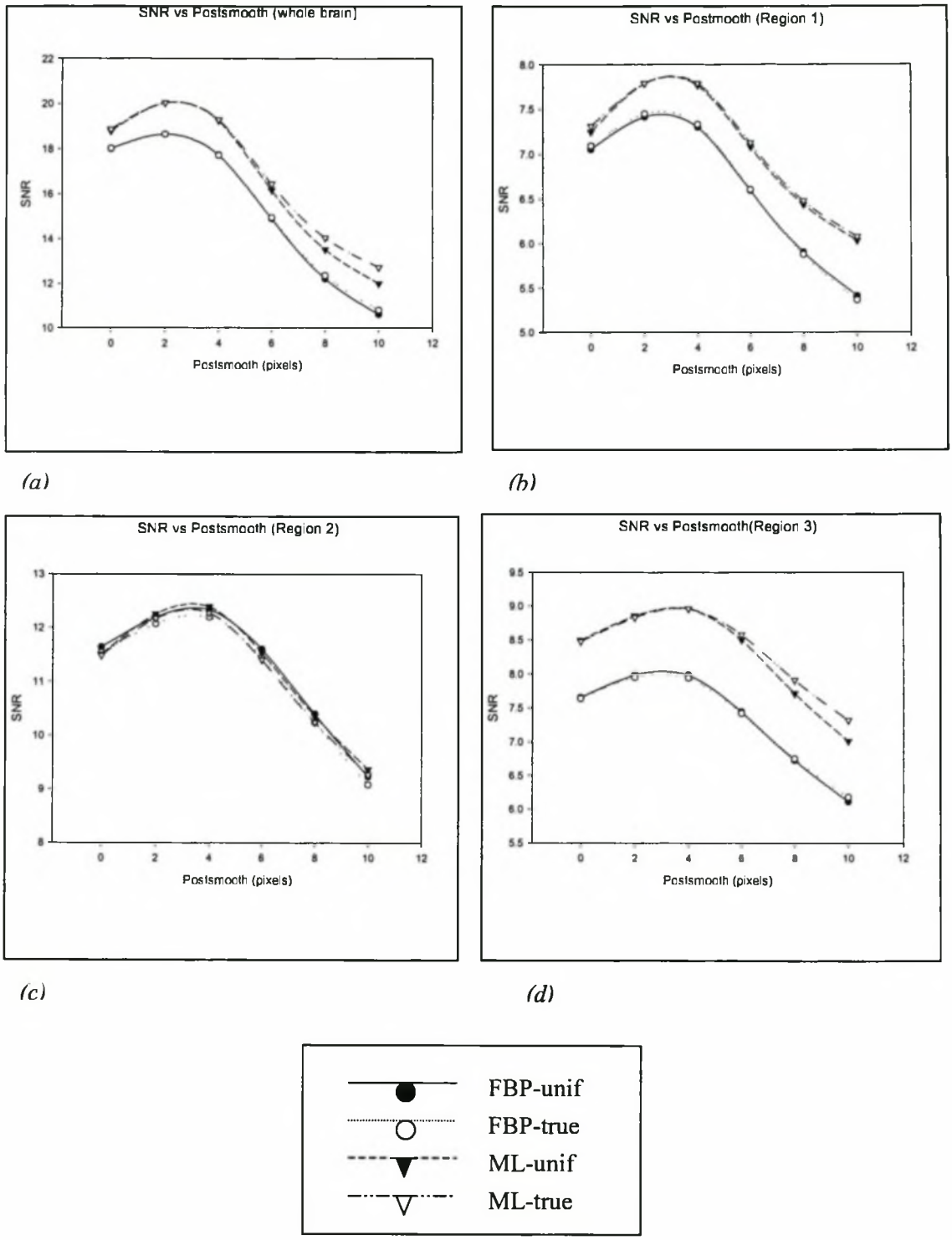

Fig 5.16 (a) – (d) Plot of SNR versus postsmooth for different regions in the brain for dataset corresponding to 100 % reduction in intensity and lesion radius = 5.2 mm.

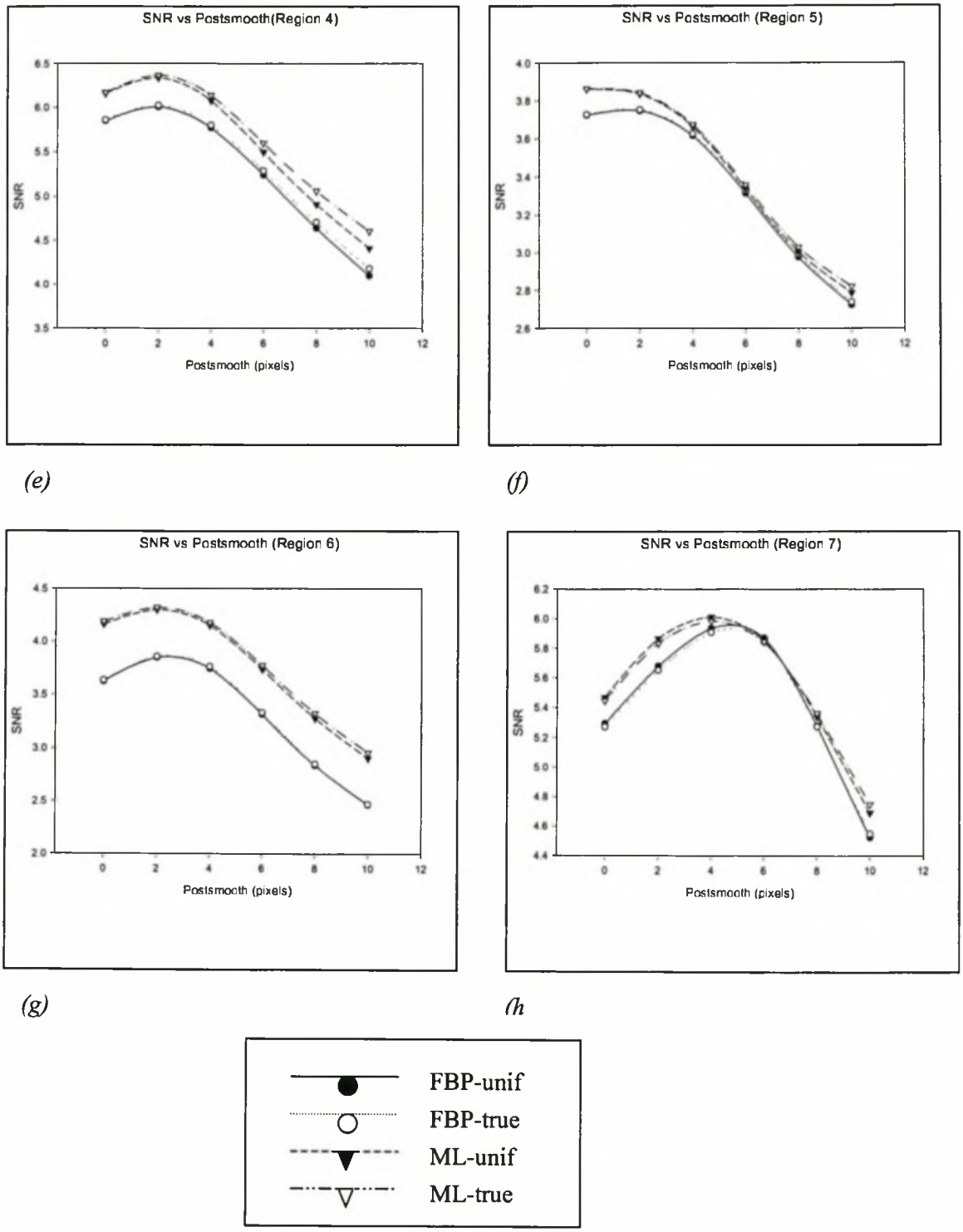

Fig 5.16 (e) – (h) Plot of SNR versus postsmooth for different regions in the brain for dataset corresponding to 100 % reduction in intensity and lesion radius = 5.2 mm.

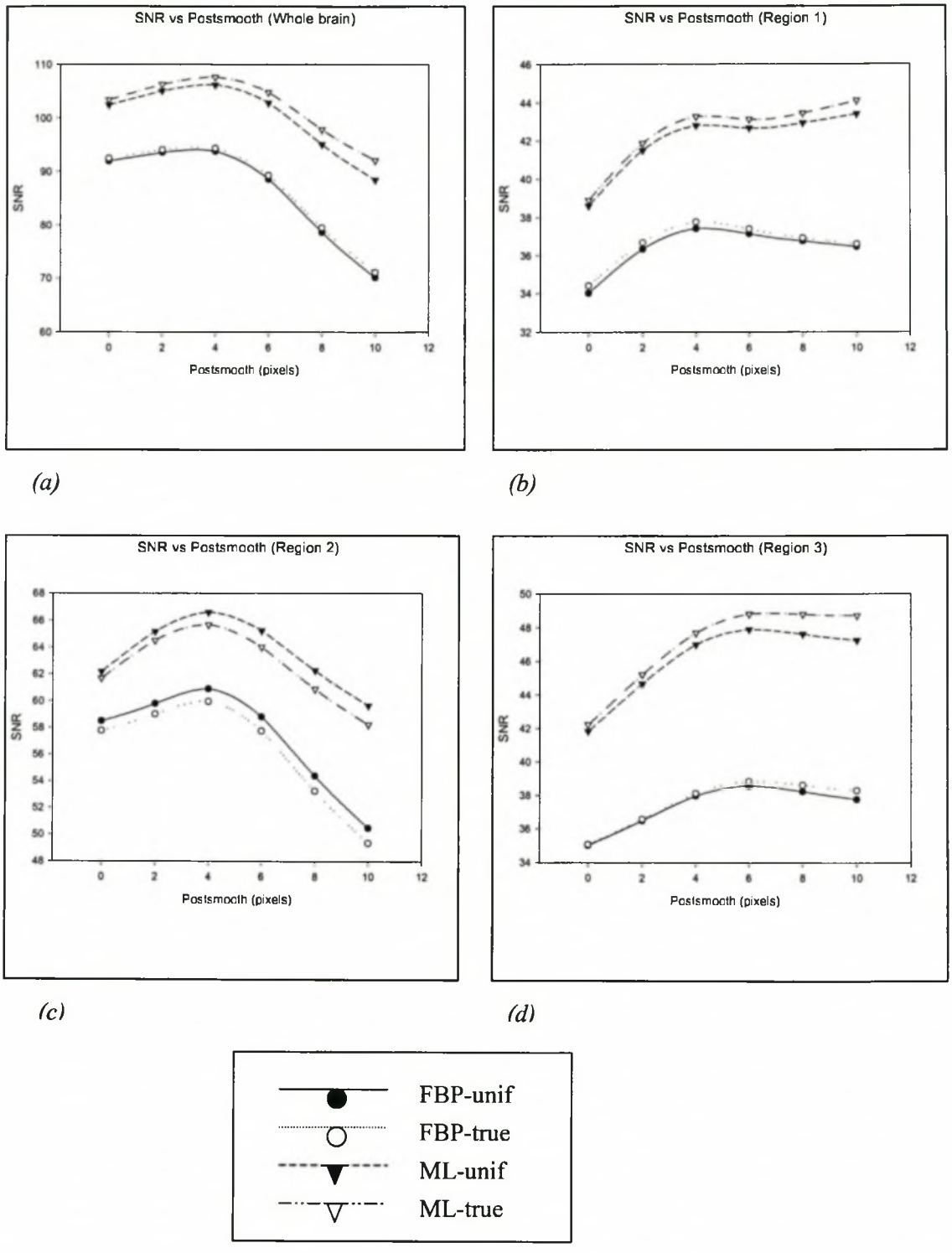

Fig 5.17 (a) – (d) Plot of SNR versus postsmooth for different regions in the brain for dataset corresponding to 100% reduction in intensity and lesion radius = 10.4 mm.

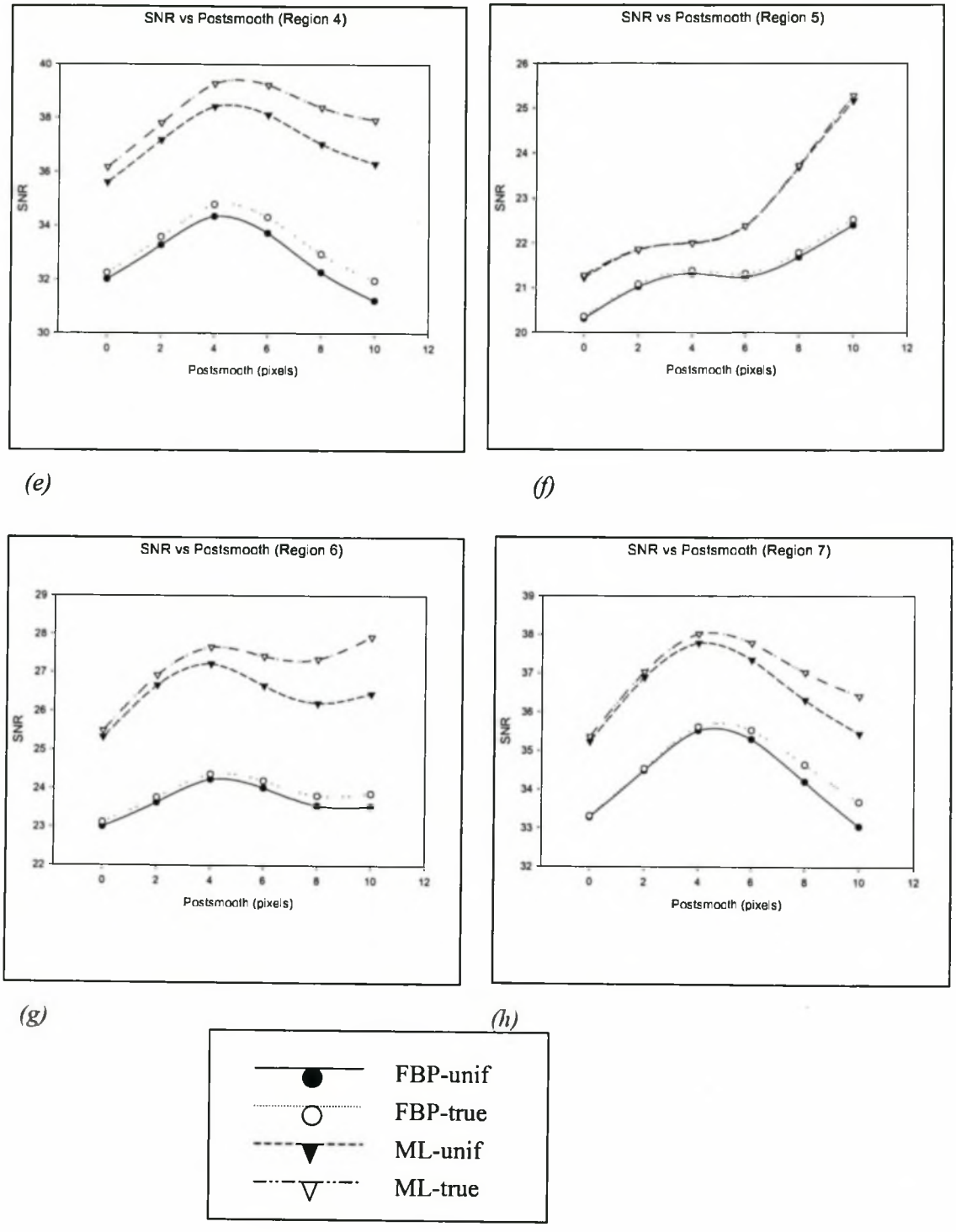

Fig 5.17 (e) – (h) Plot of SNR versus postsmooth for different regions in the brain corresponding to dataset with 100% reduction in intensity and lesion radius = 10.4 mm.

5.3.5 rms Standard Deviation versus rms Bias

Figure 5.18 shows a plot of the rms standard deviation against the rms bias (as determined from equations (4.7) and (4.5) respectively). The curves represent the region encompassing the entire brain and pertain to the baseline images, i.e. the noisy reconstructions without lesions. The curves illustrate that the rms standard deviation decreases with postsmooth at the expense of increased bias. However lower bias and standard deviation values are shown for the ML methods.

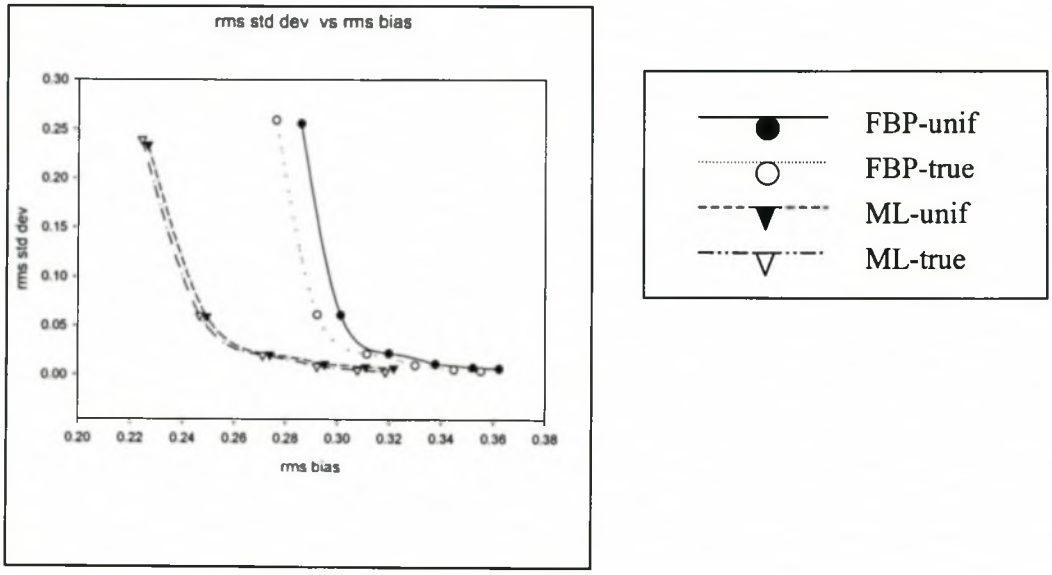

Fig 5.18 Plot of rms standard deviation versus rms bias of the whole brain. The points of the curve indicate a postsmooth of 0, 2, 4 ,6 ,8 and 10 pixels

5.3.6 Mean Differences between baseline and "ground truth" image

The mean differences were calculated from equation (4.8) and presented in Table 5.1. This simulates a normal clinical setting where 2-D regions are drawn over a particular area of interest. The table shows that the difference is smallest with the ML-true method. The difference from the true image is greatest with the FBP methods.

Region	FBP-unif (%)	FBP-true (%)	ML-unif (%)	ML-true (%)
1	-19.97	-17.65	-6.63	-4.24
2	-33.08	-30.90	6.69	8.66
3	-33.53	-31.60	-10.04	-8.68
4	-30.33	-28.95	-5.61	-3.96
5	-32.71	-30.74	-11.71	-9.80
6	-31.82	-30.44	-11.04	-9.72

Table 5.1 The mean difference between baseline and "ground truth" image

The next chapter presents an in-depth discussion of the results obtained in both experiments.

Chapter 6

Discussion

6.1 Introduction

This chapter provides a critical analysis of the results presented in Chapter 5. The discussion follows the sequence listed below.

6.2 Phantoms and attenuation maps

6.3 Influence of attenuation correction techniques on brain SPECT studies

6.4 Influence of reconstruction techniques on brain SPECT studies

For the purpose of this discussion, the set of images and curves specifying the case of 100 % reduction with lesion radius of 5.2 mm is referred to as dataset I. Dataset II corresponds to 100 % reduction in intensity with lesion radius of 10.4 mm.

6.2 Phantoms and Attenuation Maps

The activity maps are displayed in Figure 5.2 and Figure 5.11 for Experiments I and II respectively. These represented the "ground truth" images. The digital phantoms could be easily adapted to model pathology or variations in normal anatomy, allowing control over factors such as Poisson noise, intensity values and lesion sizes. The SPECT activity maps in both experiments were constructed from MRI data. The high resolution nature of the phantom permitted careful analysis of different reconstruction methods for lesion detection.

Figure 5.3 represents the attenuation map derived from the PET transmission scan and used in Experiment I. A profile of this attenuation map is shown in Figure 5.4. Transmission scanning is considered the gold standard [5], [6], [42] for the

determination of attenuation coefficients. Ideally, a SPECT transmission scan would have been preferable, although it also contains noise, but was unavailable at the time of the experiment. The advantage of using the PET scan is that it was based on a real measurement of attenuation in the brain. However, as previously stated, the original PET transmission scan contained noise which was transposed to the SPECT attenuation image used in the creation of the phantom data.

The attenuation map created from the segmented MRI data was used in Experiment II and displayed in Figure 5.12. This attenuation map reflects a more clinical, realistic situation. Attenuation coefficients vary in the region of the skull and bone as depicted by the white areas in the Figure 5.12. The central portions appear more uniform and resemble, more closely, the characteristics of true brain attenuating properties as measured with CT.

The uniform attenuation map was constructed in exactly the same way for both experiments and three slices are presented in Figure 5.13. Since attenuation in soft tissue is similar to attenuation in water, the value of 0.15 cm^{-1} [43] was chosen as the attenuation coefficient. This represents the narrow beam attenuation coefficient for 140 keV photons. At some institutions, a linear attenuation coefficient of 0.11 cm^{-1} or 0.12 cm^{-1} is used. This compensates for the detection of scattered photons within the total absorption peak by mathematically under-correcting for attenuation. In these experiments, the effect of scatter was excluded.

6.3 Influence of Attenuation Correction on Brain SPECT images

It is accepted that transmission-based non-uniform attenuation correction can supply more accurate absolute quantification [6], [44]. It is, however, unclear whether the approximation by a uniform attenuation map provides specific disadvantages in the routine clinical practice of lesion detection of functional brain SPECT imaging. The discussion that follows aims to fulfil the objective of determining the effect of uniform attenuation correction. The comparison in this section is between FPB-unif versus FBP-true, and ML-unif versus ML-true.

6.3.1 The Reconstructed Data

One set of noisy reconstructions for each of the two experiments is displayed in Figure 5.5 (Experiment I) and Figure 5.14 (Experiment II). Overall comparison of images reconstructed with FBP-unif and FBP-true shows no appreciable differences. In addition, no visual differences were observed in areas whose attenuation properties differed from soft tissue. This can be seen in the region of the cerebellum and temporal poles. The same applies when images reconstructed using ML-true and ML-unif are compared. This suggests that the use of a uniform attenuation map provides no qualitative changes to the reconstructed data.

6.3.2 Signal to Noise Ratio (SNR)

The variation of SNR as a function of postsmooth is shown in Figures 5.7 and 5.8 for Experiment I and Figures 5.16 and 5.17 for Experiment II. From Figures 5.16 and 5.17, the overall impression is that there is very little separation of the curves comparing FBP-unif to FBP-true.

Region 5 for both experiments display no noticeable difference in SNR curves when comparing FBP-unif with FBP-true and ML-unif with ML-true. This is mostly a homogeneous white matter region and therefore a non-uniform attenuation map will offer minimal advantages in this area.

Certain regions (regions 1, 6, 7) pertaining to Experiment I, dataset I, show improvement in SNR with FBP-true. Dataset II of Experiment I (Figure 5.8) demonstrate a larger difference when comparing FBP-true with FBP-unif. This could possibly be due to the larger lesion size extending to mixed areas of the brain, sometimes including skull and bony regions, and not being confined to a particular area of homogeneity.

The regions (e.g. Experiment I, region 7) that showed appreciable differences when comparing FBP-unif with FBP-true and ML-unif to ML-true were located close to bony structures. One explanation is that, in these regions, the uniform attenuation map and the true non-uniform attenuation map have the largest difference. Another explanation is that these regions are shallow. The bone (whose higher attenuation coefficient is ignored) is relatively a larger contributor to attenuation than in the case of deeper regions, where other tissues also contribute largely to attenuation.

Interestingly, certain regions pertaining to Experiment I (dataset I, region 1 and 6 and dataset II, region 1, 2 and 7) show that the FBP-true is better than ML-unif. This suggests that the attenuation properties of the brain contribute greatly to the reconstructed image. This will imply that to improve the reconstructed data, a significant step would be to improve the attenuation map and not necessarily the

reconstruction technique. The data was inspected by running 20 simulations using a smoothed transmission scan. This revealed that the noise in the PET transmission scan had a greater impact on the reconstructed data than expected. These findings were also observed by Kemp *et al* [45] and Kritzman ***et al*** [46]. The study by Kemp attempted to rectify this by segmenting the PET transmission scan.

The problem in Experiment I is that the calculated attenuation map assumes uniform attenuation, which may be a reasonable assumption in reality. However, this was not the case of Experiment I. The sinograms were produced with the true attenuation map which, due to noise in the transmission scan, represented non-uniformities in the brain. The effect of this was particularly harmful when the uniform attenuation map was utilised in the reconstruction. This explains the substantial difference in SNR between ML-true and ML-unif. Based on this simulation study, there was no conclusive evidence regarding the influence of the attenuation correction technique on the detection of lesions.

Experiment II was formulated to produce a more accurate and realistic attenuation map. The results of Experiment II, dataset I show very little separation of the curves when comparing FBP-true with FBP-unif and ML-true with ML-unif. Greater separation of the curves were observed in Experiment II, dataset II (lesion radius = 10.4 mm) with the true methods always performing better than the uniform methods. This can be validated by regions 1, 3, 4, 6 and 7. The difference appeared more pronounced in dataset II since the lesion size was bigger which, in some instances, incorporated other non-homogeneous areas of the brain. Region 7 is a cranial lesion with more bony structures. As expected, the use of the true attenuation map improved

the performance of the algorithm. Region 1 is located in the temporal pole of the brain. Regions 1 and 7 are shallow, thus the reconstructed data will suffer the effects of the use of a uniform attenuation map and produce inferior reconstructed data. This area is of particular interest since epilepsy is most likely to affect the region of the temporal pole.

6.3.3 Bias and Variance Measurements

Using these two parameters, the different algorithms were compared by varying the smoothing parameter for each method. The general trend for rms bias and rms standard deviation measurements are displayed in Figure 6.1.

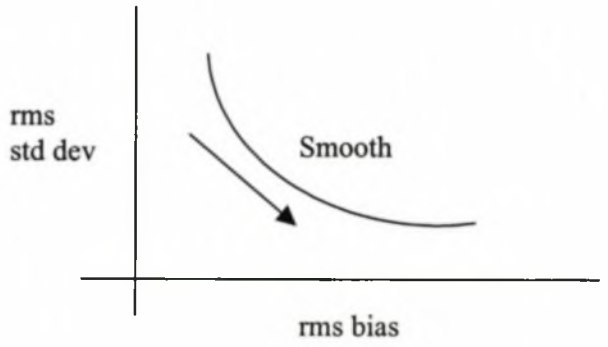

Fig 6.1 Schematic representation of general bias-standard deviation

While bias characterises the systematic deviation of the reconstruction from the true image, the standard deviation characterises the random variation of the reconstruction around its average. Generally, smoothing decreases the rms standard deviation at the expense of increased bias as illustrated in Figure 6.1

The curves displayed in Figure 5.9 and Figure 5.18 represent the rms bias and rms standard deviation curves for Experiment I and Experiment II respectively. These

curves conform to the general trend of bias - standard deviation measurements where smoothing decreases the standard deviation but causes an increase in the bias. When comparing the different algorithms, it is observed that at the same standard deviation, the bias is lower when the true attenuation maps are used. This indicates that the true methods perform superiorly when compared to the uniform methods of reconstruction.

6.3.4 Maximum Difference in SNR

SNR and bias versus standard deviation curves demonstrated that in some regions of the brain, the use of the true attenuation map improved the detection of lesions. However, it was uncertain if this difference was significant. The percentage difference was quantified using equation (5.1). The maximum difference of 2.3 % was computed when FBP-unif was compared to FBP-true and 4.9 % was obtained in the case of the ML methods. These maximum difference values were observed at a postsmooth of 10 pixels (26 mm). Due to the extreme loss of resolution, the use of a smoothing kernel with a FWHM of 10 pixels may be too strong for most clinical applications. Between 2 and 4 pixels (5.2 mm and 10.4 mm) the maximum difference in SNR was calculated to be 1.5 % (FBP) and 1.7 % (ML). With regard to SPECT imaging, a difference of less than 2 % will contribute very little to lesion detection. This difference may be significant if absolute quantification is performed, however, the focus of this study was on lesion detection.

6.4 Influence of Reconstruction Methods of Brain SPECT images

The second research question regarding the impact of the reconstruction technique on lesion detection is investigated. The discussion that follows compares the ML methods with the FBP methods.

6.4.1 The Reconstructed Data

One set of noisy reconstructions for each of the two experiments are displayed in Figures 5.5 (Experiment I) and Figure 5.14 (Experiment II). An observation is that the ML methods produce images that exhibit more noise than the FBP methods despite the fact that the images have been postsmoothed with the same smoothing kernel. This is more evident in Figure 5.5. A possible explanation is that the backprojector in FBP inherently performs blurring due to its interpolation resulting in a slightly smoother image in comparison to the ML methods.

6.4.2 Signal to Noise Ratio (SNR)

From Figure 5.7 (Experiment I) the first observation is that, in the absence of smoothing, FBP outperforms the ML method. It is well known that the ML image is subjectively a very poor one [47]. This is because the ML algorithm strictly enforces agreement with the projection data, and noisy data produces noisy ML images. The application of Gaussian smoothing improves SNR and the ML methods perform better than the FBP methods. Several methods have been suggested to deal with noise in the reconstructed data. One approach is to apply stopping rules, as proposed by Llacer and Veklerov [48] where the iterative method is halted before the image deteriorates. Another approach is to perform regularisation using an additional function besides the likelihood, forcing the final reconstruction to be a compromise

between strict agreement with the data and agreement with *a priori* knowledge of the image. Nuyts and Fessler [49] compared the noise properties using a penalized likelihood method as opposed to postsmoothing the ML reconstruction. This study found that the two regularization methods performed similarly for applications where a shift-invariant spatial resolution was imposed.

The second observation is that SNR peaks between 2 and 4 pixels (5.2 and 10.4 mm) and then decreases as postsmoothing increases. The application of some Gaussian smoothing reduces the noise in the data.

From the SNR curves of Experiment II (Figure 5.17 and 5.18) a significant difference is noted between the ML and FBP methods with the ML methods always outperforming the FBP methods. The reason for this is that FBP is an approximation, whereas the iterative algorithm monotonically approaches the estimates of the unknown parameters by maximising the probability of the data given the parameters.

6.4.3 Bias and Variance

The curves of Experiment I (Figure 5.9) illustrate that, in the absence of smoothing, FBP methods demonstrate a much lower variance when compared to the ML methods. This is due to the noise in the image when reconstructed with ML methods. However, postsmoothing causes a rapid decrease on the rms standard deviation. These findings were also observed by Nuyts [50] The curves show that ML methods produce the lowest bias at the same rms standard deviation.

These observations lead to the conclusion that iterative methods improve lesion detection when compared to FBP methods of reconstruction.

6.5 Other observations

SNR and postsmoothing

SNR peaks at a postsmooth of between 2 to 4 pixels. The effect of smoothing on the MLEM reconstruction method is shown in Figures 5.6 and 5.15 for Experiments I and II respectively. Without smoothing, the image is very noisy with minimal definition of structures. Figure 5.15 demonstrates this more explicitly. A smoothing kernel of 2 pixels (5.2 mm) reduces the noise and produces an image where the structures in the brain can be identified. Although SNR is best at a smoothing of 4 pixels (10.4 mm), visually this smoothing produces an image that lacks detail for clinical purposes. The reason for this discrepancy is that, in these experiments, computer observers are used rather than human observers. Computer observers are known to perform differently from human observers [51]. It would have been impractical for the large number of images to be inspected by humans.

Figure 5.17 displays the curves for Experiment II dataset II. Regions, 1, 3, 5 and 6, demonstrate an increase in SNR up to a postsmooth of 4 pixels, followed by a slight decrease and finally a progressive increase in SNR with postsmoothing. Inspection of the hypo-perfused phantom demonstrated that as postsmoothing increases, the adjacent lesions smooth into each other, causing a summation effect. The lesion of concern is thus perceived as a single large lesion rather than two independent smaller lesions. This is due to the close proximity of the lesions to each other causing it to be influenced by neighbouring lesions. The second increase in SNR was therefore an

artefact of the simulation and not a feature of Gaussian smoothing. If the lesions were placed further from each other, the same effect would have been observed but only at larger smoothing kernels. One solution would be to simulate each lesion individually, but this would increase the computation time by a factor of 8, which was unfeasible for this experiment.

SNR as a function of % reduction in intensity

SNR for 50 % and 100 % reduction in intensity was compared. The curves for the 50% reduction in intensity performed similarly to the 100 % reduction and are thus not displayed. However, it was observed that SNR increases when there is a greater degree of hypo-perfusion. This is to be expected, since the signal relative to the background is higher with a greater reduction in intensity.

SNR as a function of lesion size

Figures 5.16 and 5.17 compares the ML-true methods with a lesion size of 5.2 mm and 10.4 mm respectively. Higher SNR is observed when the lesion size is increased. The numerical observer (and possibly also human observers) detects that which is proportional to the entire signal. This is the integral of the difference between an image with and without lesions. The integral is increased if the lesion size is larger. In this case, the size of the signal is increased, therefore the probability of finding the lesion is greater. This would also apply if the lesion is more intense. The same explanation applies when comparing SNR in Figures 5.7 and 5.8.

Difference between mean image and 'ground truth" image

The mean image over all noise realisations using the data set without lesions was compared to the "ground truth" image. Six two-dimensional regions of interest were drawn at different locations. This was performed to simulate a standard clinical setting. The difference in the means was calculated and shown in Table 5.1. These values provide an indication of the degree of the bias in the mean of a region. The maximum difference is 9.8 % with the ML-true method and 11.71 % with the ML-unif method. The FBP methods show a maximum difference of 31.60 % (FBP-true) and 33.53 % (FBP-unif). This large difference with the FBP methods further illustrates that the ML algorithms perform superiorly and the use of the true attenuation map only adds a slight improvement to the quality of the image.

Another observation from Table 5.1 is that the bias is negative with FBP using Chang's attenuation correction method. The reason for this is that Chang's method is only an approximation. In his original paper, Chang proposed that the process should be iterative [8]. A simulation was run to check if the bias remained negative if the Chang method was used iteratively. The simulation showed that with one iteration, Chang method underestimated the activity resulting in a negative bias. This negative bias approached zero in subsequent iterations which indicated that FBP using Chang's method systematically underestimated the activity. Nevertheless, the reconstructions performed are of interest, since non-iterative FBP is used at most institutions including Tygerberg Hospital.

Chapter 7

Conclusions

7.1 General Conclusions

In the case of brain SPECT imaging, the use of uniform attenuation correction shows slight deterioration (less than 2%) in the reconstructed data. This difference was only visualised in the regions within the vicinity of bony structures. The investment in a transmission source to improve attenuation correction in brain SPECT imaging would offer very little benefit to the detection of lesions and does not warrant implementation at Tygerberg Hospital at this stage.

Marked improvement in lesion detection was observed when iterative reconstruction algorithms were used. The implementation of iterative techniques together with appropriate smoothing can improve the quality of reconstructed brain SPECT images.

In view of these findings, it is strongly recommended that iterative reconstruction techniques should be implemented at Tygerberg Hospital to improve the detection of lesions for brain SPECT studies.

7.2 Suggestions for future work

1. This investigation was performed on simulated datasets. Before implementation, the investigation should be evaluated on a well-defined patient population.

2. The effects of scatter were excluded in the simulated data. It would be interesting to see if correction for scatter improved SNR in the case of brain SPECT imaging.

3. The projection data was determined by simulating collimator blurring by means of Gaussian diffusion. However, no correction for collimator blurring was incorporated in the reconstruction algorithms. These and other issues are being examined in the current research efforts at Tygerberg Hospital.

4. The methods of iterative reconstruction demonstrated excessive noise in the absence of smoothing. Several approaches to reduce the noise using penalised likelihood ML, postsmoothing ML or applying inter-iteration filtering have been suggested, but more work in the area is clearly needed.

5. Recommendations have been made to improve the reconstructed data by using *a priori* information. One approach would be to use anatomical information derived from CT or MRI images. Some work in this field has already been completed for PET images. Extending the study to determine the influence of *a priori* information in the case of SPECT studies would provide interesting as well as useful research.

Appendix

Gaussian Smoothing

The Gaussian smoothing operator is a 2-D convolution operator that is used to blur images and reduce noise. It is similar to the mean filter, but it uses a different kernel that represents the shape of a bell. The degree of smoothing is determined by the standard deviation of the Gaussian.

The Gaussian distribution in 1-D has the form Equation Section 1

$$G(x) = \frac{1}{\sqrt{2\pi}\sigma} e^{-\frac{x^2}{2\sigma^2}} \tag{1.1}$$

where σ is the standard deviation of the distribution with mean 0.

In 2-D, an isotropic Gaussian has the form:

$$G(x,y) = \frac{1}{2\pi\sigma^2} e^{-\frac{x^2+y^2}{2\sigma^2}} \tag{1.2}$$

References

1 Holman BL, Devous MD Sr. Functional brain SPECT: the emergence of a powerful clinical method. *J Nucl Med* 1992; 33: 1888-1904.

2 Catafau AM, Lomena FJ, Pavia J, Parellada E, Bernardo M, Setoain J, Tolosa E. Regional cerebral blood flow pattern in normal young and aged volunteers: A 99mTc-HMPAO SPET study. *Eur J Nucl Med* 1996; 10: 1329-37.

3 Licho R, Glick SJ, Xia W, Pan TS, Penney BC, King MA. Attenuation compensation in ^{99m}Tc SPECT brain imaging: a comparison of the use of attenuation maps derived from transmission versus emission data in normal scans *J Nucl Med* 1999; 40: 456-463.

4 Larsson A, Johansson L, Sundstrom T, Ahlstrom KR. A method of attenuation and scatter correction of brain SPECT based on computed tomography images. *Nuclear Med Commun* 2003; 24: 411-420.

5 Bailey DL. Transmission Scanning in Emission Tomography. *Eur J Nucl Med* 1998; 25: 774-787.

6 Van Laere K, Koole M, Verspijt J, Dierckx R. Non-uniform versus uniform attenuation correction in brain perfusion SPET of healthy volunteers. *Eur J Nucl Med* 2001; 28: 90 – 98.

7 Sorenson JA, Phelps ME. *Physics in Nuclear Medicine*. 2nd ed. Philadelphia: WB Saunders Company, 1987, 408-417p.

8 Chang LT. A method for attenuation correction in radionuclide computed tomography. *IEEE Trans Nucl Sci* 1978; 25: 638-643.

9 Rowell NP, Glaholm J, Flower MA, Cronin B, McReady VR. Anatomically derived attenuation coefficients for use in quantitative single photon emission tomography studies of the thorax. *Eur J Nucl Med* 1992; 19: 36-40.

10 Zaidi H, Montandon M, Slosman DO. Magnetic resonance imaging-guided attenuation and scatter corrections in three dimensional brain positron emission tomography. *Med. Phys* 2003; 30: 937-948.

11 Shepp LA, Vardi Y. Maximum likelihood reconstruction for emission tomography. *IEEE Trans Med Imaging* 1982; 1: 113-122.

12 Lange K, Carson R. EM reconstruction algorithms for emission and transmission tomography. *J Comput Assist Tomogr* 1984; 8: 306-316.

13 Dempster AP, Laird NM, Rudin DB. Maximum likelihood from incomplete data via the EM algorithm. *J R Stat Soc* 1977; 39: 1-38.

14 Chornoboy ES, Chen CJ, Miller MI, Miller TR, Snyder DL. An evaluation of maximum likelihood reconstruction for SPECT. *IEEE Trans Med Imaging* 1990; 9: 99-110.

15 Kauppinen T, Koshkinen MO, Alenius S, Vanninen E, Kuikka JT. Improvement of brain perfusion SPET using iterative reconstruction with scatter and non-uniform attenuation correction. *Eur J Nucl Med* 2000; 27: 1380-1386.

16 Gutman F, Gardin I, Delahaye N, Rakotonirina H, Hitzel A, Manrique A, Guludec D, Vera P. Optimisation of the OSEM algorithm and comparison with FBP for image reconstruction on a dual head camera: a phantom and a clinical ^{18}F-FDG study. *Eur J Nucl Med Mol Imaging* 2003; 30: 1510-1519.

17 Blocket D, Seret A, Popa N, Schoutens A. Maximum likelihood with ordered subsets in bone SPECT. *J Nucl Med* 1999; 40: 1978-1984.

18 Hine GJ ed. *Instrumentation in Nuclear Medicine. Vol I.* New York-London: Academic Press, 1967, 495-500p.

19 Rollo DF ed. *Nuclear Medicine Physics, Instrumentation, and Agents.* Saint Louis: The C V Mosby Company, 1977; 236 -237p.

20 Moore SC, Kouris K, Cullum C. Collimator design for single photon emission tomography. *Eur J Nucl Med* 1992; 19: 138-150.

21 Knoll GF. *Radiation Detection and Measurement* 3rd Ed. New York: John Wiley and Sons Inc 1999, 265-274p.

22 McCarthy AW, Miller MI. Maximum likelihood SPECT in clinical computation times using mesh-connected parallel computers. *IEEE Trans Med Imaging* 1991; 10: 426-436.

23 Weishi X, Lewitt RM, Edholm PR. Fourier correction for spatially variant collimator blurring in SPECT. *IEEE Trans Med Imaging* 1995; 14: 100-115.

24 Blokland KAK, Reiber HC, Pauwels EKJ. Quantitative analysis in single photon emission tomography. *Eur J Nucl Med* 1992; 19: 47-61.

25 Zaidi H, Montandon M. Which attenuation coefficients to use in combined attenuation and scatter corrections for quantitative brain SPET. *Eur J Nucl Med* 2002; 29: 967-969.

26 Nuyts J. *Nuclear Medicine Technology and Techniques: Lecture Notes.* Catholic University Leuven, 2000

27 Bruyant P. Analytic and iterative algorithms in SPECT. *J Nucl Med* 2002; 43: 1343-1358.

28 Thomas GB and Finney RL. *Calculus and Analytic Geometry*. 6th ed. London: Addison Wesley Publishing Company; 1984; 570-577p.

29 Hutton Brian. A clinical perspective of accelerated statistical reconstruction. *J Nucl Med* 1997; 24: 797-808.

30 Bowsher JE, Valen EJ, Turkington TG, Jaszczak RJ, Floyd CE, Coleman RE. Bayesian reconstruction and use of anatomical a priori information for emission tomography. *IEEE Trans Med Imaging* 1996; 15: 673 – 686.

31 Hudson HM, Larkin RS. Accelerated image reconstruction using ordered subsets of projection data. *IEEE Trans Med Imaging* 1994; 13: 601-609.

32 Maes F, Collignon A, Vandermeulen D. Multimodality image registration by maximisation of mutual information. *IEEE Trans Med Imaging* 1997; 16: 187-198.

33 [Online]. BrainWeb. http://www.bic.mni.mcgill.ca/brainweb (26 November 2003).

34 Collins DL, Zijdenbos AP, Kollokian JG, *et al*. Design and construction of a realistic digital brain phantom. *IEEE Trans Med Imaging* 1998; 17: 463-468.

35 [Online] Statistical Parametric Mapping. http://www.fil.ion.ucl.ac.uk/spm (26 November 2003).

36 Owunwanne A, Patel M, Sadek S. The handbook of radiopharmaceuticals. London: Chapman and Hall Medical, 1995, 65p.

37 [Online] NIST Physics Laboratory. http://physics.nist.gov/PhysRefData/XrayMassCoef/tab4.html (26 November 2003)

38 International Commission on Radiological Units and Measurements. *Tissue Substitutes in Radiation Dosimetry and Measurement Report 44*. Bethesda MD: ICRU; 1989.

39 [Online] Harvard Medical Web http://www.med.harvard.edu/JPNM/physics/511keV/fun_phys/fun_phys.html (26 November 2003).

40 Wagner RF, Brown DG. Unified SNR analysis of medical imaging systems. *Phys Med Biol* 1985; 30: 489-518.

41 K Baete, J Nuyts, W Van Paesschen, P Suetens, P Dupont. Anatomical based FDG-PET reconstruction for the detection of hypometabolic regions in epilepsy. *Proceedings of the IEEE NSS and MIC*, Norfolk, 2002.

42 Stodilka RJ, Kemp BJ, Prato FS, Kertesz A, Kuhl D, Nicholson RL. Scatter and attenuation correction for brain SPECT using attenuation distributions inferred from a head atlas. *J Nucl Med* 2000; 41: 1569-1578.

43 Harris CC, Greer KL, Jaszczak RJ, Floyd CE Jr, Fearnow EC, Coleman RE. Tc-99m attenuation coefficients in water filled phantoms determined with gamma cameras. *Med Phys* 1984; 11: 681-685.

44 Rajeevan N, Zubal G, Ramsby SQ, Zoghbi SS, Seibyl J, Innis RB. Significance of nonuniform attenuation correction in quantitative brain SPECT imaging. *J Nucl Med* 1998; 39: 1719-1726.

45 Kemp BJ, Hamblen SM, Lowe VJ. An evaluation of segmented attenuation correction for PET. *Proc SNM 48th annual meeting*, 2001:196.

46 Kritzman JN, Fessler JF, Corbett EPF. Artifact recognition for transmission tomography systems [abstract]. *J Nucl Med* 2001; 42: 195p

47 Barret HH, Wilson DW, Tsui BMW. Noise properties of the EM algorithm: I. Theory. *Phys Med Biol* 1994; 39: 833-846.

48 Llacer J, Veklerov E. Feasible images and practical stopping rules for iterative algorithms in emission tomography. *IEEE Trans Med Imaging* 1989; 8: 186-193.

49 Nuyts J, Fessler JA. A penalized likelihood image reconstruction method for emission tomography, compared to postsmoothed maximum-likelihood with matched spatial resolution. *IEEE Trans Med Imaging* 2003; 22:1042-1052.

50 Nuyts J. On estimating the variance of smoothed MLEM images. *IEEE Trans Med Imaging* 2002; 49: 714 – 721.

51 Barrett HH, Yao J, Rolland JP. Model observers for the assessment of image quality. *Proc Natl Acad Sci Colloquium Paper*, 1993: 9758-9765p.